Interaction of non-metallic inclusions,microstructure, and fatigue loading with small crack growth in high-strength steels

Andrew Roiko

A? Aalto University

Interaction of non-metallic inclusions, microstructure, and fatigue loading with small crack growth in high-strength steels

Andrew Roiko

A doctoral dissertation completed for the degree of Doctor of Science (Technology) to be defended, with the permission of the Aalto University School of Engineering, at a public examination held at the lecture hall K216 of the school on 27 October 2017 at 12:00.

Aalto University
School of Engineering
Department of Mechanical Engineering
Engineering Materials

Supervising professor
Prof. Hannu Hänninen, Aalto University School of Engineering, Finland

Thesis advisor
Prof. Gary Marquis, Aalto University School of Engineering, Finland

Preliminary examiners
Prof. Arto Lehtovaara, Tampere University of Technology, Finland
Prof. emer. Gunnar Härkegård, Norwegian University of Science and Technology, Norway

Opponents
Prof. Gregory Glinka, University of Waterloo, Canada
Prof. Arto Lehtovaara, Tampere University of Technology, Finland

NORDIC ECOLABEL

441   697
Printed matter

Abstract

The increased demand and requirements for high-strength steels drives the need to better understand and predict the fatigue endurance and crack growth challenges related to their use in critical machine components. Non-metallic inclusions or defects in the steel become increasingly important as the hardness or strength of the steel increases. The distribution and the ability to predict the largest inclusion that causes failure is crucial for the proper and successful design and production of the components.

The extreme value distribution is effective in predicting the maximum inclusion in a volume of steel. The proper prediction and use of inclusion data gathered from polished specimen as well as differences in anisotropy are important to consider when gathering data for use in design and prediction of fatigue life or failure. The difference in non-metallic inclusions and the forging direction affects the distribution of the size of the inclusions as well as the fatigue endurance limit and its scatter of the steel. The extreme value distributions combined with the Murakami-Endo model are used as a design approach for fatigue failure for components with ultra-long fatigue lives and step loading. This design approach uses the master curve for Optically Dark Area (ODA) growth obtained by Murakami et al. and combines it with the prediction of the largest non-metallic inclusion along with the estimate of the fatigue life of the component.

The initiation and growth of small cracks from inclusions as well as small Focused Ion Beam (FIB) notches behave in a similar manner and show a strong tendency to follow the local microstructure. The effect of the local microstructure on the small fatigue crack growth is studied using FIB milling to create cross-sections of the microstructure. This showed that the microstructure is also linked to the formation of ODA around non-metallic inclusions in ultra-long fatigue. The behaviour of a small crack growing from notches in high cycle fatigue is studied by using high-speed microscopy and Rumul fatigue testing machines. The test results show that small cracks initiate and grow quickly in the beginning of the fatigue life after which they propagate slowly at a stress intensity range lower than the large crack growth threshold until it is reached.

Comparing different data results for different R-ratios shows that the parameter $\Delta K+$ works well to compare the crack growth rate of small cracks in the studied quenched and tempered steel. For crack arrest the $\Delta K+$ or K_{max} thresholds are lower for cracks with higher compressive loading. Also test results showed that increasing only the compressive portion of loading can reinitiate arrested

Preface

It all began with a research proposal for clean steels and fatigue survival with material imperfections. The original research project, called FATE-DEFEX, was initiated with the cooperation between Industry partners, Aalto University (formerly known as Helsinki University of Technology (HUT)) and the Technical Research Centre of Finland VTT, along with the Finnish Funding Agency for Innovation (TEKES) overseeing and providing the majority of the funding for research. This 3 year project kicked off in 2008. Based on the body of work produced in this project and building upon it in two consecutive projects MACY and SCarFace (Short Crack and Fretting fatigue damage in mechanical engineering) (in the years 2011-2015) this thesis and the publications presented in it have been produced.

This thesis, like many human endeavors is one of work and perseverance that would not be possible without the supporting foundation of family, friends, and companions. I wish to thank first my supervisor Prof. Hannu Hänninen, who has made this all possible and offered me this opportunity. I would also wish to thank my work mentor, college and patient coauthor Jussi Solin, who provided me with an abundance of opportunity and guidance, and was so many countless times ready and willing to help. I would also like to thank Jouni Alhainen and Teemu Sarikka, as well as the staff of the Engineering Materials laboratory and VTT for their help. Special thanks are also in order to Prof. Yukitaka Murakami for his guidance and advice. His counsel and teaching have been important in my work. I also wish to thank all the researchers and staff I worked with at Kyushu University for their kind hospitality and support.

I wish to thank my wife Anna-Kaisa, for her unwavering support and love. I am grateful as well, for the support and encouragement from all my family and friends. Thank you all for the help in times of need, for it has made all the difference.

Espoo, October 3, 2017

Andrew Lauri Roiko

Contents

List of publications

This thesis is based on the following original publications which are referred to in the text as I–VI. The publications are reproduced with kind permission from the publishers.

I A. Roiko, H. Hänninen, H. Vuorikari, Anisotropic distribution of non-metallic inclusions in a forged steel roll and its influence on fatigue limit, International Journal of Fatigue, Volume 41, August 2012, Pages 158-167, ISSN 0142-1123

II A. Roiko, Y. Murakami, A design approach for components in ultralong fatigue life with step loading, International Journal of Fatigue, Volume 41, August 2012, Pages 140-149, ISSN 0142-1123

III A. Roiko, J. Solin, Measurement of small cracks initiating from inclusions, Focused Ion Beam notches and drilled holes, International Journal of Fatigue, Volume 62, May 2014, Pages 154-158, ISSN 0142-1123

IV A. Roiko, J. Solin, T. Sarikka, H. Hänninen, The paths of small fatigue cracks in high-strength steels initiated from inclusions and small defects, Accepted at: Materials Performance and Characterization on 21.4.2017

V A. Roiko, J. Solin, H. Hänninen, Behavior of small cracks under negative stress ratio fatigue loading, International Journal of Fatigue, Volume 104, 2017, Pages 379-388, ISSN 0142-1123

VI A. Cetin, A. Roiko, M. Lind, Towards proper sampling and statistical modelling of defects. Fatigue & Fracture of Engineering Materials & Structures, Volume 38, September 2015, Pages 1056-1065, ISSN 1460-2695

Author's contributions and original features

The experimental methods along with the analysis of the obtained data presented in this thesis for small crack growth at high and ultra-long cycle fatigue are used to better understand, measure and model small crack behaviour and growth with respect to loading, microstructure, and the defect or non-metallic inclusion distribution in high-strength steels. The following are the features believed to be original:

1.   The author performed all the experimental as well as the majority of the data analyses of the experimental results which include the examination of the extreme value distribution of the inclusions located at the site of fatigue crack initiation on the fracture surface of the fatigue test bars. This is compared with the extreme value distribution of the inclusions found on polished specimen. The extreme value distribution of the non-metallic inclusions is used to predict the theoretical lower fatigue limit of the steel. The data obtained from the inclusion analyses and fatigue tests provided new results on the role of anisotropy in the extreme value distribution of inclusions in forged steel and the effect this has on the fatigue limit and scatter of the steel.

2.   The author wrote a brief review of previous work on the origin and formation of Optically Dark Area (ODA) in ultra-long life fatigue. The author also contributed a new design approach, proposed for calculating the effects of different loading levels on ultra-long fatigue life using the ability to predict the presence of non-metallic inclusions in steels with extreme value methods combined with the master curve of ODA growth to determine the maximum threshold stress for ultra-long fatigue life using the $\sqrt{(area\ )}$ parameter model.

3.   The author developed a specialized test method to study the initiation and growth of micro-cracks from small defects. This new method along with the majority of the analyses of the results performed by the author provided new and original data about the initiation and growth of small cracks from defects near the fatigue endurance limit.

4.   The author used a new investigation method of FIB milling and imaging to investigate the connection between the microstructure and growth path of small cracks in high cycle fatigue. The general preferential growth direction and formation of ODA is linked to adjacent grain orientations and sub-grain structures such as martensite lath and packet orientation. Local martensite laths and packets in the microstructure surrounding a non-metallic inclusion give additional explanation to the formation and origin of the ODA which is an original and new result obtained by new and original methods.

5.   The author tested and measured the growth of small cracks initiated from microscopic notches and loaded near the crack growth threshold under

varying stress ratios. These results of small crack growth under different negative stress ratios are unique and provide new insights into the interaction between small cracks, defects, and loading.

6.   The experimental portion of the publication was the extent of the author's contribution to the publication.

List of abbreviations

ASTM	American Society for Testing Materials
EDS	Energy Dispersive X-ray Spectroscopy
FIB	Focused Ion Beam
FS	Fracture Surface
GCF	Giga Cycle Fatigue
GEV	Generalized Extreme Value
HCF	High Cycle Fatigue
HV	Vickers Hardness (kgf/mm^2)
LEFM	Linear Elastic Fracture Mechanics
LEVD	Largest Extreme Value Distribution
MML	Maximum Likelihood
MPa	Mega Pascal
ODA	Optically Dark Area
PDF	Probability Density Function
PS	Polished Specimen
QT	Quenched and Tempered
SEM	Scanning Electron Microscopy
UHCF	Ultra-High Cycle Fatigue

List of symbols

h_o	The average $\sqrt{area}$ of the maximum inclusion distribution obtained from the standard inspection area
$\sqrt{area_{max,j}}$	The maximum size of the largest inclusion determined for a standard inspection area S_o or volume V_o
$\sigma_w{}'$	The modified $\sqrt{area}$ model for ODA predicted lower bound fatigue limit
D_G	The standard deviation for the Gumbel distribution
$\sqrt{area}$	The square root projected area of an inclusion or defect on the plane normal to the stress
$\bar{\lambda}$	The mean of the Gumbel distribution
σ_a	The stress amplitude
σ_{max}	The maximum stress
σ_{min}	The minimum stress
σ_{wl}	The $\sqrt{area}$ model predicted lower bound fatigue limit
σ_{wu}	The predicted upper fatigue limit
ΔK_{ODA}	Stress intensity factor range for ODA
$\Delta\sigma_+$	The positive portion of the stress range
ΔK_{th}	Threshold stress intensity factor range
$\Delta\sigma$	The stress range
A	A parameter determined experimentally for predicting the largest inclusion
B	A parameter determined experimentally for predicting the largest inclusion
C	A constant used to calculate the fatigue limit
d_s	The standard deviation for the normal distribution
K_{max}	The maximum stress intensity factor
L	The calculated likelihood
n	The number of trials used for calculation of binomial probability
N_f	The number of stress cycles to failure

p	Binomal probability of an event
P_{conf}	The confidence of an unknown calculated probability
r	The number of failures for calculation of binomial probability
R	The stress ratio, $\sigma_{min}/\sigma_{max}$
R_o	Runout
S	Area of prediction (mm^2)
S_{max}	The maximum value of the stress amplitude
S_o	Standard inspection area (mm^2)
T	Return period
V	Volume of prediction (mm^3)
V_o	Standard control volume (mm^3)
V_s	Control volume for prospective fatigue failure (mm^3)
Y	Geometry correction factor
α	$0.226 + HV \times 10^{-4}$
ΔK_+	The positive portion of the stress intensity factor range
δ	Scale parameter used in extreme value theory
λ	Location parameter used in extreme value theory
σ	The stress acting on a specimen

1. Introduction

Machines that are used under demanding loads are commonly subject to fatigue failure. This failure is caused by the initiation and growth of small fatigue cracks from defects in the component that eventually result in the complete failure of the machine. This problem is examined here from three viewpoints: 1) the defect that initiates small crack growth (in steels generally a non-metallic inclusion), 2) the material surrounding the defect (in this case the microstructure), and 3) the effect of loading on initiation and small crack growth that makes up the majority of high and ultra-long cycle fatigue life.

Non-metallic inclusions are intrinsic to steel components. The cleanliness of the steel has been improved during the last 50 years due to the development of better production methods and technology that allow steel mills to minimize the impurities that result in defects and inclusions in the steel. The use and application of steels has also increased and the demands and design requirements have called for stronger and harder steels for lighter and more efficient machine components. This increase in the use of high-strength steels has resulted in the need for more specific and in-depth understanding of the challenges that are presented for harder and stronger steels. A general rule is: the higher the tensile strength the lower the ductility of the steel. This means that the size of defects or stress concentrators in the steel become more critical as the strength or hardness of the steel increases. This problem is seen in the correlation of the fatigue strength of steels to the hardness. Generally the fatigue strength of the steel increases until around 400 HV after which the scatter increases and the correlation is no longer valid.

Non-metallic inclusions can be of different types and sizes. The location, size and distribution of the non-metallic inclusions needs to be understood so that it is possible to predict for large components with large volumes the largest non-metallic inclusion conservatively. The theory that has been used to predict extremes (in this case maxima extremes) is called extreme value theory.

The research relating to small crack fatigue growth has been ongoing for many decades. The commonly referred Kitagawa-Takahashi diagram defines the basic relationship between small cracks that arrest and long cracks that behave according to

Linear Elastic Fracture Mechanics [1]. The application of linear elastic fracture mechanics to small cracks as well as studies about small crack growth were made by Smith in ref [2] and Taylor in ref [3] as well as many others [4-9]. The general conclusion is that this area is challenging and many researchers have concluded that there are certain intrinsic factors such as the relationship of the crack size to the microstructure that dominate this portion of the crack growth. The general understanding of the majority of the research is that the small cracks grow faster than long cracks and the explanation for this varies. Certainly there are differences in material as well as test methods, however the fact remains that the successful modelling of small crack growth is difficult and is also subject to many variables and interpretations.

One of the main reasons why small crack growth has been difficult to study is due to the lack of proper tools to perform reliable and repeatable measurements of very small cracks that are tested for very long fatigue lives. The in-situ high-speed optical microscopy combined with FIB notches and small drilled holes provides a novel as well as reliable and consistent method of measuring the growth of the small crack during long and continuous fatigue testing. Furthermore, the experimental setup used here provides a window into the behaviour of small cracks under large compressive fatigue loads in the high cycle fatigue regime. This type of testing gives insight as well as data about the effect of compressive stress on the behaviour of small cracks initiating and growing in many industrial machine components that use various surface hardening production methods to improve the fatigue life of the components.

1.1 Non-metallic inclusions in steel and fatigue endurance limit

The fatigue endurance limit of steels is calculated or estimated using different assumptions for the mechanism causing fatigue crack initiation. The steel can be defect free which would mean that a fatigue limit of this type of steel would be the upper limit, or as is generally the case a steel can have defects of varying sizes in its matrix which would result in a lower fatigue limit. The fatigue life or fatigue limit for steels is often studied with respect to the distribution of non-metallic inclusions in the steel. The connection between the distribution of defects in metallic materials and their fatigue properties has been discussed in many publications (see references: [10-33]). The general approach that has evolved to deal with this problem is based on the probabilistic modelling of the distribution of the inclusions. The occurrence of the largest inclusions in the steel is predicted by studying different cross-sections of steel and recording the sizes of the maximum inclusions found. Then by applying the theory of extreme values it is possible to predict the occurrence of the largest inclusion that will cause fatigue failure. The inclusion distribution model is then applied in a crack growth rate model which is used to calculate the distribution of cycles to failure or the decrease in the fatigue limit of the material. This kind of a predictive model is outlined in refs: [19] [20] [28].

1.1.1   Inclusion analysis

Non-metallic inclusions that occur in steels can be divided into two categories; indigenous and exogenous. Indigenous inclusions occur in steels as a result of the reactions that take place between the chemical compounds present in the steel as it cools and solidifies. The exogenous inclusions are inclusions that occur in steels due to the result of mechanical incorporation from the slag or other materials and impurities that the molten steel comes into contact with.

The forming of the indigenous inclusions happens by precipitation that is a result of the reactions occurring in the molten steel. The formation of these indigenous inclusions which are composed mostly of oxides and sulphides can be controlled by the use of additives to the steel, or by changes in the solubility during the cooling and solidification of the steel.

Exogenous inclusions are more variable in their occurrence and composition. Some of the main characteristics of these types of inclusions are greater size, increasing randomness in occurrence, irregular shapes and complexity in structure. The compositions of exogenous inclusions are typically oxides, which is due to the nature of the source of the inclusions such as the slag. [34]

During the production of wrought steel components there is a large degree of anisotropy that is produced depending on the amount of forging that is performed. The forging strengthens the component by refining the grain structure, but also can have an effect on the size distribution and direction of the non-metallic inclusions in the steel. This effect of anisotropy is studied in publication (I) and the difference in the sampling direction can be seen in the inclusion distribution. This effect is then reflected in the fatigue limit and its scatter. There is clearly a larger population of inclusions that are found when sampling perpendicular to the forging direction than parallel to the forging direction.

The data about the inclusions in the steel that is gathered from testing and analysis can be described using different types of distributions. Some of the typical parent distributions that are used are: normal, Poisson, binomial, exponential, and lognormal distributions. The method of extreme value analysis takes either the maximum or minimum values from the different types of original or parent distributions that were listed.

The largest inclusions found in steels can be considered to be the extreme maximum of the general population of inclusions. To choose which type of extreme distribution model to use the GEV, Fréchet, and Gumbel extreme value distributions were tested with a Kolmogorov–Smirnov test using the inclusion data. In publication (I) the best fit of these three was found to be the Gumbel distribution which is the extreme value distribution for the normal distribution. This extreme value distribution is given as follows:

$$P(X \leq x) = exp\left\{-exp\left(-\frac{x-\lambda}{\delta}\right)\right\} \tag{1}$$

where the values λ and δ are the location and scale parameters [32] [35]. For the Gumbel distribution the mean ($\bar{\lambda}$) is calculated as follows:

$$\bar{\lambda} = \lambda + \delta \cdot \gamma \tag{2}$$

where γ is calculated as:

$$\gamma = -\int_0^1 \left(\ln\left(\ln\left(\frac{1}{x}\right)\right)\right) dx \approx 0.57721 \tag{3}$$

The standard deviation (D_G) for the Gumbel distribution is:

$$D_G = \frac{\delta \cdot \pi}{\sqrt{6}} \tag{4}$$

The distribution parameters of a Gumbel distribution for the inclusion populations studied were estimated by using the Maximum Likelihood Method (MML). This method uses the probability density function to directly calculate the parameters of a distribution by calculating whether a certain probability distribution function can describe a set of data. The parameters of the probability distribution are fitted to maximize the likelihood which is calculated as follows:

$$L = \prod_{i=1}^n f(x_i) \tag{5}$$

In equation (5) the function $f(x_i)$ is the Probability Density Function (PDF). The Gumbel probability density function is given as:

$$f(x, \lambda, \delta) = \frac{1}{\delta} \cdot exp\left\{-\frac{(x-\lambda)}{\delta}\right\} \cdot exp\left\{-exp\left\{-\frac{(x-\lambda)}{\delta}\right\}\right\} \tag{6}$$

To estimate the parameters λ and δ of the distribution by MML method the logarithm of the MML is usually used for simplicity. This equation is called the log likelihood and is given as:

$$\ln(L) = \sum_{i=1}^n ln\{f(x_i)\} \tag{7}$$

The maximization of equation (7) is done with an iterative process. The two parameters λ and δ are manipulated to maximize ln(L) in equation (7). Once the maximum log likelihood ln(L) is known then the parameters λ and δ that produced the MML are the parameters that best fit the distribution according to MML method.

When the λ and δ maximum likelihood estimates for the Gumbel distribution are known these values are used to estimate the maximum size of the inclusion $\sqrt{area_{max}}$ with a return period T and it is given as:

$$x(T) = \lambda + \delta \cdot y \tag{8}$$

where y = -ln(-ln[(T-1)/T]) with the return period T being defined as V/V_o, where V_o is the inspection volume and V being the volume of the part for which the maximum inclusion is being predicted. In this case V_o is calculated as follows: $S_o \cdot h_o$, where h_o is the average $\sqrt{area}$ of the maximum inclusion distribution obtained from the inspection. The calculation of V for a test bar that is placed under rotating bending loading is considered to be the volume where the local stress is greater than 90% of the nominal stress. Murakami proposes in Ref. [28] the following volume: V = $0.05\pi d^2 l$, where d is the diameter of the gauge length and *l* is its length for rotating bending fatigue test specimen used in publication (I).

1.2   The statistical aspects of fatigue for high-strength steels

The scatter in the fatigue strength of high-strength steels is mostly caused by the scatter of the size of the inclusions that are in the specimen [28]. The scatter in the size of the inclusions present in the steel is caused by two main factors. The first factor is the volume of steel that is in question, and the second is the distribution of the inclusion sizes in the steel.

The distribution of inclusion sizes has been researched and a method for inclusion rating based on extreme value statistics has been developed [36,37]. This method can also be found in the ASTM standard E 2283-03 and can be implemented as follows:

The maximum size $\sqrt{area_{max,j}}$ of the largest inclusion is determined for a standard inspection area S_o or volume V_o. This process is repeated n times and the resulting maximum inclusions are ranked as follows: $\sqrt{area_{max,1}} \leq \sqrt{area_{max,2}} \leq \cdots \leq \sqrt{area_{max,j}}$. The cumulative distribution function F_j(%) as well as the reduced variates y_j for the inclusion distribution are then calculated according to the following equations:

$$F_j = j \times 100/(n+1) \tag{9}$$

$$y_j = -ln\{-ln[j/(n+1)]\} \tag{10}$$

The maximum size $\sqrt{area_{max,j}}$ is then ploted according to the ranking that was done on a probability plot with the abscissa coordinates as $\sqrt{area_{max,j}}$ and the ordinate axis being either F_j or y_j. An example of this kind of a plot is shown in Figure 1.

As can be seen in Figure 1 the reduced variate plotted against the $\sqrt{area_{max,j}}$ has a linear relationship. This relationship can be used to predict for a larger volume of steel. The linear relationship can be written as follows:

$$\sqrt{area_{max}} = A \cdot y + B \tag{11}$$

where $y = -ln\{-ln[j/(n+1)]\}$. To predict the maximum inclusion in an area S or volume V we get: T = S/So or V/Vo and since we know that T=1/(1-F), so by using the previous equations we can write equation (11) as:

$$x(T) = B - A \cdot ln\{-ln[1 - 1/T]\} \tag{12}$$

This equation can be used to predict the largest inclusion in a given volume of steel. The parameters A and B are determined experimentally [28].
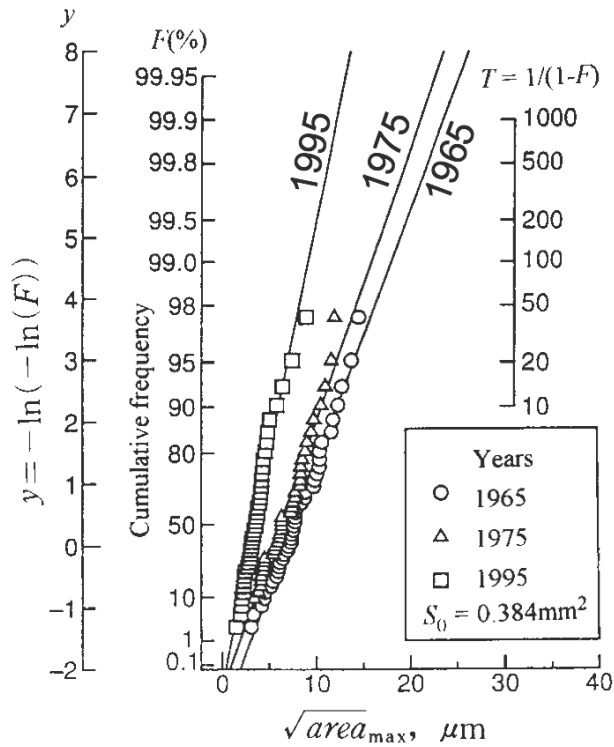

Figure 1. The results show the improvement in production quality for SAE52100 steel for different years with respect to the distribution of the maximum inclusions in the steel [28].

This standard method has been in use for many years, however there are improvements and changes that could be done to improve it. Some possible improvements are proposed in publication (VI).

1.3   Fatigue endurance limit prediction

The fatigue limit of steel is empirically estimated with fatigue tests. The staircase test method is used to estimate the fatigue limit of the steel. Two different methods are used for the analysis of test data. The first is the Maximum Likelihood Method (MML) that has been developed by Dixon and Mood for the staircase test [38], which uses the method of least squares to estimate the fatigue limit and its standard deviation from the data. The second method analyses the data with the binomial probability theory to estimate the fatigue limit of the steel. This method has been developed by Wallin [39].

1.3.1   Maximum likelihood analysis

The calculation of the fatigue endurance limit is done using a special case of the Maximum Likelihood Method, which is commonly called the method of least squares. This method is the minimization of the following equation which is called the sum of the squares:

$$S = \sum_{i=1}^{n} \left(\frac{x_i - \bar{x}}{d_s} \right)^2 \tag{13}$$

The average $\bar{x}$ and the standard deviation d_s are assumed to be from the normal distribution and are fitted to the data so that equation (13) is minimized. This method has been developed by Dixon and Mood and is used for the analysis of the staircase test results. [38]

1.3.2   Binomial probability analysis

The results of the staircase test resemble a binomial distribution because the test specimen either fails at the stress level or it survives. The probability of having a certain number of failures at a certain stress level can be calculated according to the binomial theory as:

$$P(X = r) = \binom{n}{r} \cdot p^r \cdot (1 - p)^{n-r} \tag{14}$$

where

$$\binom{n}{r} = \frac{n!}{r!(n-r)!} \tag{15}$$

Equation (14) gives the discrete probability that there are (r) failures in (n) trials. In a staircase test the probability of the event p is not known. This probability can be calculated with a certain confidence (P_{conf}) with the following equation:

$$P_{conf}(p \leq x) = \frac{\int_{p=0}^{x} \binom{n}{r} \cdot p^r \cdot (1-p)^{n-r} \cdot dp}{\int_{p=0}^{1} \binom{n}{r} \cdot p^r \cdot (1-p)^{n-r} \cdot dp} \qquad (16)$$

The results can then be ranked according to binomial probability which starts at zero. The ranking gives the P_{conf} level of 5%, 50%, and 95 % for each stress level. [39,40]

1.3.3   The Murakami-Endo model

The Murakami-Endo Model predicts that when the location of the fracture origin is a small defect or non-metallic inclusion then the fatigue limit of the material can be determined by the Vickers hardness of the microstructure surrounding the non-metallic inclusion and the square root of the projected area $\left(\sqrt{area}\right)$ of the defect normal to the stress. [28]

The model treats the inclusions or defects that are smaller than $\sqrt{area} \leq 1000\ \mu m$ as small cracks and it has been tested to be valid for high-strength steels (HV $\geq$ 400). The general equation is given as:

$$\sigma_{wl} = C \cdot (HV + 120)/\left(\sqrt{area}\right)^{1/6} \qquad (17)$$

where C is 1.43 for inclusions on the surface of a test specimen, 1.41 for inclusions in touch with the surface and 1.56 for inclusions underneath the surface. The σ_{wl} is the predicted fatigue limit (MPa), HV is the Vickers hardness of the matrix around the inclusion (kgf/mm^2), $\sqrt{area}$ is the square root projected area of the inclusion on the plane normal to the stress (μm). This method for calculating the lower fatigue limit has also been applied and used successfully for steels and metals with a micro hardness that is less than 400 HV. [28]

1.4   Small crack growth in high cycle fatigue

The study of small crack growth has been approached from different viewpoints. A general approach has been to examine the fatigue endurance limit with respect to the defect or size of the crack. This approach is schematically illustrated using the Kitagawa-Takahashi (KT) diagram shown in Figure 2. The x-axis is the size of the crack, and the y-axis is the threshold stress range. This graph shows that for the smallest cracks as the size approaches zero there is no longer any correlation between the stress range and crack size. This means that for many steels there is a part of the curve where the size of the crack will cause failure independent of the loading.
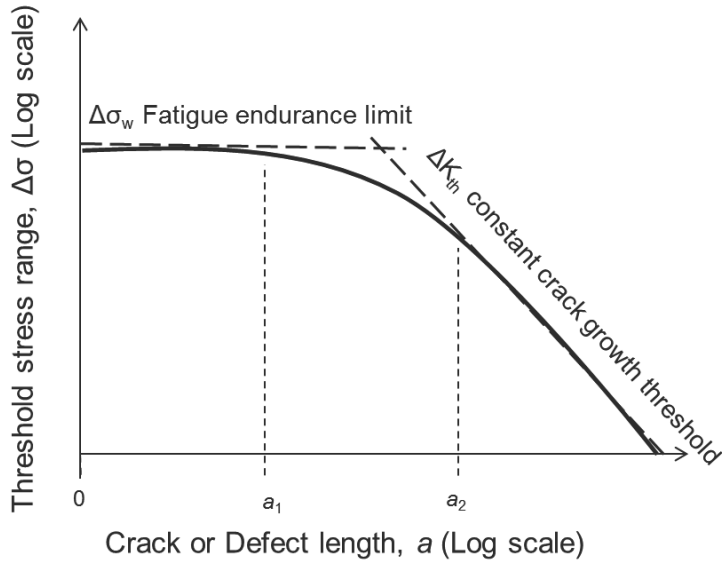
Figure 2. A schematic of the Kitagawa-Takahashi diagram. [1]

The KT diagram shows the fatigue endurance limit for small cracks and the fatigue crack growth threshold for long cracks. The existence of a fatigue endurance threshold can be interpreted to mean that below a certain size of defect or crack found in the material, in this case a_1, the material will fail if a stress range above the endurance limit is applied. An interpretation of these results was done by El Haddad et al. who proposed an intrinsic crack length ' l ' to be added to short cracks [41]. This publication offers a possible theoretical explanation to the short or small crack portion of the KT diagram, it does not however explain the phenomena itself, nor does the theory of an intrinsic crack length have any basis in the material itself.

Using the KT diagram assumes that there is actually a true threshold for fatigue endurance. This has usually been typically set at 10^7 fatigue cycles which is considered to be the runout limit for High Cycle Fatigue (HCF). With many machine components this amount of loading cycles is achieved early in the design life. This has led to more research into what is known as Ultra-High Cycle Fatigue (UHCF) or Giga Cycle Fatigue (GCF) which is fatigue cycles of more than 10^7 as well as up to and beyond 10^9 cycles. The KT diagram has to assume an endurance limit for the crack growth. If a higher number of cycles are assumed for an endurance limit it can be that this would also eliminate or reduce the small crack portion of the KT diagram.

1.4.1   Small crack growth and loading

The designer of machines or mechanical components that experience numerous loading cycles needs to understand the material response to the loads and possible defects or cracks that can grow or initiate fatigue cracks. This has given rise to many studies about small fatigue cracks and unique phenomena that occur in their initiation and growth. The effect of the compressive portion of the fatigue cycle on the behavior of small cracks is important for many industrial components that, for example, use various surface hardening treatments to improve their fatigue strength or endurance. Many fatigue improving treatments cause high compressive stresses on the component surface. This can prevent fatigue, but if not used properly, cause failure.

One important factor to consider is the impact of different mean stresses on the growth of small cracks. This area of research has been concentrated more on the positive portion of the R-ratio. In this study we observe what impact an increasing and large compressive loading ratio has on the initiation and growth of small cracks.

The general focus of most small crack growth research has been in the range of tension - tension loading (R > 0), symmetric loading at R = -1, and other researchers have studied also the initiation and arrest of short cracks from notches under fully compressive loading [5,42-50]. An interesting question is the amount of crack closure in small cracks because the original studies done on crack closure by Elber were performed on large cracks in soft metals [51,52]. More recently Silva studied the effect of compressive loading on crack growth. One of the main focuses of his research was the inability to explain some of the effects of compression on the crack growth in fatigue by crack closure [53]. The research showed that there is a significant effect of compressive loading on the crack growth and this varies from material to material. It was concluded that some intrinsic material properties should be incorporated into models that were previously developed [54]. A recent study demonstrated using finite element analysis that the largest effect of underloads or compressive loading was the reduction of retardation effects and acceleration of crack growth [55].

The focus on the effect of compressive loading on the growth of small fatigue cracks in the quenched and tempered steel is studied in publication (V). More specifically, the effect that the compressive part of loading has on the small cracks and their growth rates near and at the threshold for crack growth. The measurements are performed at the HCF regime and introducing very small surface notches, which can initiate cracks close to or even below the fatigue endurance limit ($N_f > 10^7$) of the specimen.

1.4.2   Small crack growth and microstructure

Fatigue crack initiation and growth from surface or subsurface non-metallic inclusions in high-strength steels is of importance in many industries. This has been the focus of many studies and, in particular, a book by Murakami [28]. Some studies have found that hydrogen trapped around non-metallic inclusions provides an explanation for a cause of failure in ultra-long fatigue life of high-strength steels [28,56-63]. However, there are yet questions about the characterization and prediction of initiation and growth of microstructurally small cracks from inclusions in high-strength steels. Some reserachers have shown other factors such as the fact that cracks grow in a vacuum inside the test specimen or changes in the microstrucure around the inclusion [64-66]. Other studies have used Focused Ion Beam (FIB) milling to create cross-sections, after which FIB imaging is used to make ion channeling contrast pictures of the microstructure [67- 73]. This imaging technique has been applied to small cracks in steels to study the profile in depth [68, 74]. Researchers have recently used the FIB tools to show how the size and crystal orientation of the grains affect the growth and direction of small cracks from notches and inclusions in steel [67,68,75,76]. These tools and techniques are used to study the role the martensite sub-grain microstructure has on the initiation and growth of small fatigue cracks in high-strength steels from inclusions and notches.

Non-metallic inclusions in steel promote subsurface crack initiation, which means that the direct observation of initiation and early growth of cracks is extremely challenging. One solution is to introduce FIB-milled semielliptical notches to simulate a case, where fatigue relevant inclusions are on the specimen surface, and so the path and growth of the small crack can be observed. The small cracks which have grown from the FIB notches can then be compared with the small cracks from non-metallic inclusions that failed at or near the endurance limit. In the past there have been various definitions used to define small cracks, however, for the purposes of this study we consider small cracks to be those that are less than around 1 mm in length.

1.4.3   ODA, inclusions, and small cracks

Research into the cause of ultra-long life fatigue failure in high-strength steels has revealed that fatigue crack initiation occurs at subsurface non-metallic inclusions. Next to these subsurface inclusions a dark area is observed that is called Optically Dark Area (ODA). The presence of an ODA is not observed on fracture surfaces of specimens with short fatigue lives. The appearance of the ODA next to subsurface inclusions has been researched and documented in the following references: [22,56-58,60,77-79]. The failure of test specimen at ultra-long fatigue lives (N_f >

10^7) and the effect caused by the size of the test specimen can be united by understanding the role that non-metallic inclusions play in causing fatigue failure in ultra-long fatigue.

To predict fatigue failure due to the presence and role of the ODA and its growth from non-metallic inclusions, the work in publication (II) reviews the research that has been performed by Murakami and his co-workers in references [58,59,61,62]. The results of these studies reveal that there are several factors that have to be considered. These factors are:

1) The growth of the ODA with respect to the fatigue life of the specimen and internal hydrogen in the specimen.
2) The statistical aspect of fatigue due to the difference in volumes tested and the distribution of the maximum inclusions in the steel.
3) The dependency of the threshold stress intensity factor range ΔK_{th} on crack size.

Publication (II) reviews these three main factors involved in ultra-long life fatigue failure in high-strength steels from internal inclusions viewpoint and proposes a fatigue design approach for ultra-long fatigue lives of high-strength steel components. This design approach incorporates the effect of the volume as well as the distribution of the inclusions in the steel, along with the growth of the ODA from the inclusions in ultra-long fatigue life regimes. This design approach is only meant to be used for ultra-long life fatigue failure in high-strength steels caused by subsurface non-metallic inclusions. This design approach does not take into consideration other factors in fatigue such as mean stress, environmental effects, surface effects or notch effects.

2. Aims of the study

The goal of this thesis is to focus on the interaction of the non-metallic inclusions with the microstructure and the fatigue loading with small cracks in high-strength steels. The experiments and analyses of the results approach this problem from three perspectives:

-What is the effect of the distribution and size of the non-metallic inclusions in the steel with respect to fatigue?
This is the perspective that is studied in publications: (I), (II), and (VI).

-What is the interaction of the microstructure, inclusions, and small fatigue cracks?
Using FIB milling and imaging this perspective is investigated in publication (IV).

-What is the interaction of small fatigue cracks, loading and defects?
The research on the growth of small cracks in high cycle fatigue is investigated with special high-speed microscopy combined with small FIB notches and drilled holes in publications: (III) and (V).

3. Material and experimental methods

3.1 Material properties

3.1.1 Rotating bending fatigue testing

The test bars studied in the fatigue tests were taken from an industrial forged steel roll. The approximate dimensions of the roll are around 1 m in diameter and 6 m long. The chemical composition of the steel is given in Table 1.

Table 1. The chemical composition (wt %) of the forged steel.

	C	Mn	P	S	Cr	V	Mo	Si
Weight %	0.61	0.50	0.005	0.005	1.34	0.08	0.26	0.23

The manufacturing process of the steel roll starts with the casting of a steel ingot, after which it is forged to a degree of deformation that ranges from 4 to 7. The forged steel is pre-machined after which it is quenched and tempered, and the surface is then induction hardened and machine finished. The microhardness of the steel test bars is 320 HV.

3.1.1 Axial fatigue testing

Different batches of two steel types were studied in publications (III) - (VI). One is a bearing steel of type 100Cr6 quenched and tempered at 180 ºC to hardness 720 HV (tensile strength 1630 MPa) and the other is a quenched and tempered 34CrNiMo6 steel with a hardness of 380 HV and with 1065 MPa and 1180 MPa yield and tensile strength, respectively. In publications (III, IV and VI) the 34CrNiMo6 QT steel is from the same production batch. For publication (V) the 34CrNiMo6 QT steel is from a separate production batch and has a slightly lower tensile and yield strength given in publication (V). From here on the steel studied in publications (III, IV, and VI) will be called 34CrNiMo6 QT(A) and the steel studied in publication (V) will be called 34CrNiMo6 QT(B).

EBSD images of the microstructure of these two steels are shown in Figure 3 and the chemical composition is given in Table 2. The average ferrite grain size is 2.2 µm for the 34CrNiMo6 QT steel and around 1.4 µm for the 100Cr6 bearing steel. The estimated prior austenite grain size for the two steels was around 30 µm for the 34CrNiMo6 QT(A) steel and around 7 µm for the 100Cr6 bearing steel.
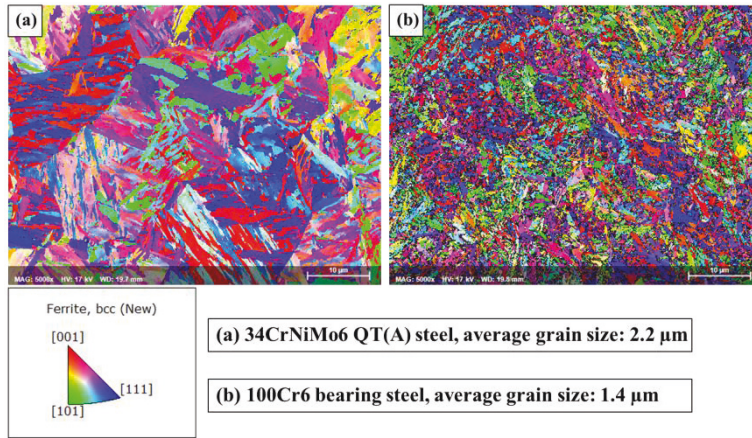
Figure 3. (a) Microstructure of 34CrNiMo6 QT(A) steel, and (b) microstructure of the 100Cr6 bearing steel. Both EBSD images are taken perpendicular to the loading direction of the test specimen.

Table 2. The chemical composition (wt %) of the 34CrNiMo6 QT and 100Cr6 steel.

Steel type	C	Si	Mn	P	Cr	Ni	S	Mo	Cu	Al
100Cr6	0.95	0.25	0.39	0.02	1.43	0.137	0.005	0.022	0.15	0.01
34CrNiMo6 QT(A&B)	0.34	0.28	0.65	0.008	1.67	1.63	0.01	0.24	0.19	0.02

3.2   Fatigue testing

3.2.1   Rotating bending fatigue testing

The fatigue properties of the steel studied in publication (I) were tested with the rotating bending fatigue test method. A Schenk rotating bending fatigue test machine was used to apply a four-point bending loading to the test bar that ensured a constant loading moment along the gauge length of the specimen. Rotation of the fatigue test bar under four-point bending results in the varying of the applied stress at a stress ratio of R = -1, at a frequency of 35 to 40 Hz. An illustration of the size and shape of the test bars is shown in Figure 4.
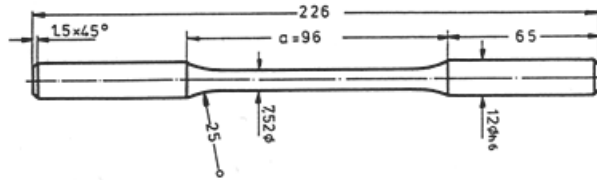
Figure 4. The geometry of the rotating bending fatigue test bar. All dimensions are in millimetres.

The fatigue test bars were removed from a forged steel roll at locations that were below the induction hardened surface. The bars that were taken tangential to the axis of the forged steel roll are called tangential test bars and correspond to the X-plane of the polished specimens used in the inclusion analysis. The test bars that were taken parallel to the axis are called axial test bars and correspond to the Y-plane of the polished specimens used in the inclusion analysis. An illustration of the direction of the test bars with respect to the steel roll is shown in Figure 5.
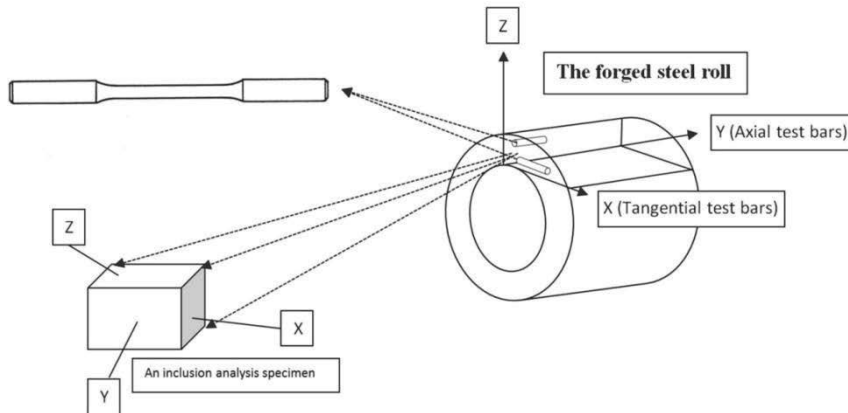

Figure 5. A schematic illustration of the location of the test bars as well as the specimens used for inclusion analysis.

After removal from the forged roll the test bars were machined and their surfaces were ground and polished. The transverse scratches were ground away and polished so that the effect of the surface features of the test bars on the fatigue limit was minimized. Testing was done using the staircase method with a step size of 5 MPa for tangential test bars and 10 MPa for axial test bars. The tests were performed at room temperature and the runout limit was set at 10^7 cycles. If a test bar reached the runout limit then the test was aborted and classified as a runout. All of the runouts were retested at a stress level that was 100 MPa higher than the runout

stress level. This was done to cause failure so that the largest inclusion causing failure could be studied.

3.2.2   Axial fatigue testing

The 100Cr6 bearing steel specimens (Figure 6) were taken from ¼ depth (17.5 mm from the surface) of a φ70 mm wrought bar. The 34CrNiMo6 QT(A&B) specimens according to Figure 7, were machined from the centreline of φ35 mm wrought bars.
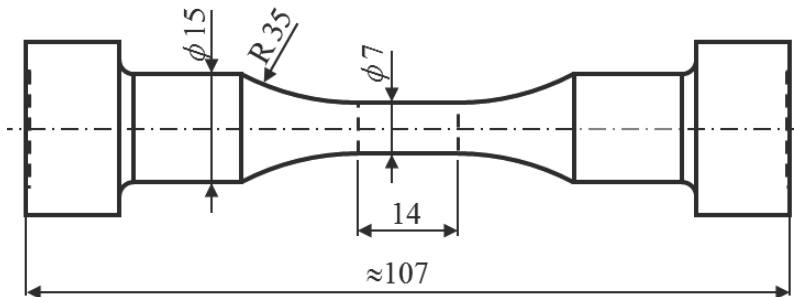

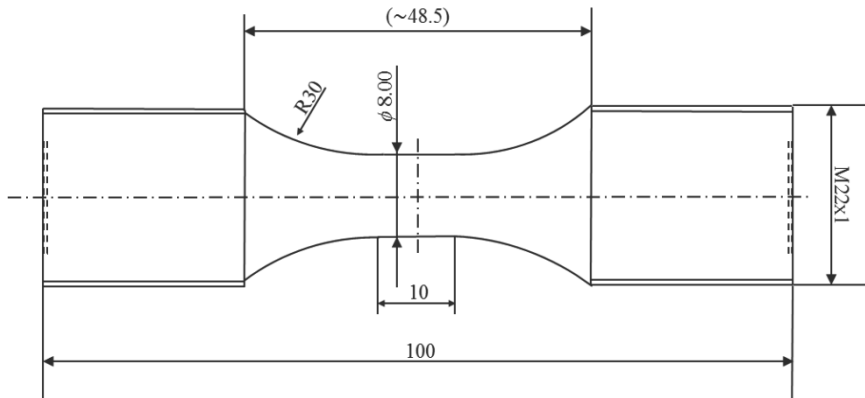Figure 6. The dimensions of the axial fatigue test bar used for the bearing steel 100Cr6.

Figure 7. The dimensions of the test bar for the quenched and tempered 34CrNiMo6 (A&B) steel used for axial fatigue testing.

The test bar shown in Figure 7 was used in publications (III)-(VI), and the test bar shown in Figure 6 was used in publication (IV).

3.3 Inclusion analysis and distribution

In publication (I) the inclusions found on the polished specimens as well as the fracture surfaces were all photographed, measured and their chemical compositions were analyzed. The elemental analysis was done using an INCA Energy 300 Microanalysis System (EDS).

The specimens used for inclusion analysis were taken from three different locations in the steel roll. The three positions were: one from close to the outer surface, one from in-between the center and the outer surface and one closer to the center of the steel roll. Once cut from the steel roll the specimens were polished. After the polishing the specimens were analyzed using an automatic INCA Feature analysis program. The program distinguishes inclusions on the polished surface by using the electron backscatter detector to differentiate between the matrix and the inclusions. The automated inspection was set at a magnification of 300X, and the inspection area that was automatically scanned and analyzed was 25 mm^2. For each plane this inspection was performed six times to achieve a total inspection area of 150 mm^2 for the plane. Once the analysis was complete the process was repeated with the same specimen on a new plane until all planes X, Y, and Z had been analyzed. This process was repeated for all three inclusion analysis specimens taken from the steel roll. A standard inspection area (S_o) of 25 mm^2 was defined for an extreme value analysis of the inclusions. The largest inclusion in each standard inspection is used for the extreme value analysis.

3.4 Small crack growth and fatigue testing

In publications (III)-(V) we apply small notches or holes to smooth specimens and investigate the relevance of using them as small crack initiators. They were used to measure small crack growth rates and thresholds. This testing method is compared to small defects such as non-metallic inclusions in the steel.

Axial fatigue testing is performed at resonant frequencies around 100 Hz and the specimens were fatigued either close to the range of smooth specimen fatigue limit or at different R-ratios that are in the high-cycle fatigue regime. The small notches were optically monitored and video recorded for crack initiation, growth and arrest in real time. An example of this is shown in Figure 8. The high-speed video microscope is a Keyence VW-9000E system that uses a high-speed monochrome camera unit, VW-600M and a zoom lens (100X to 1000X), VH-Z100R.
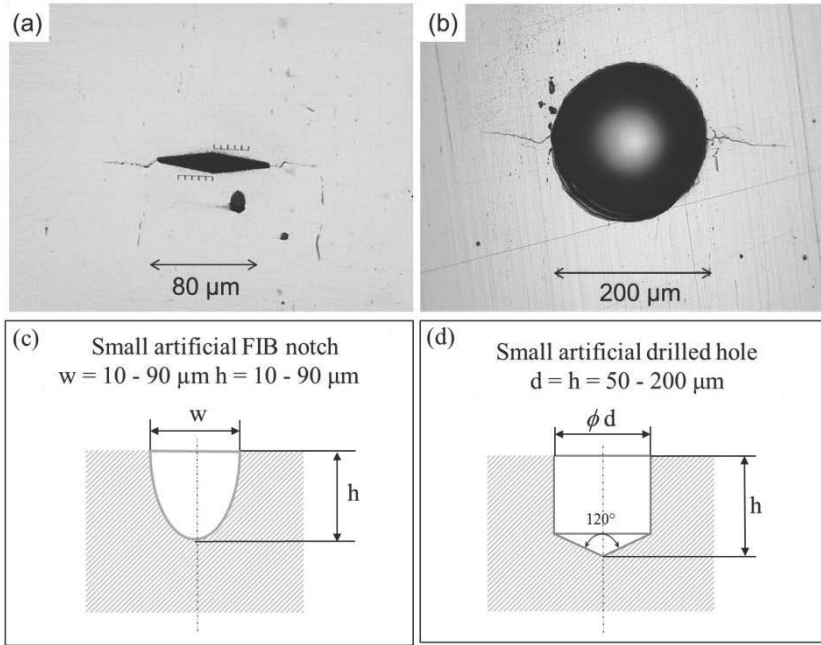
Figure 8. Examples of a) a FIB notch and b) a drilled hole being observed in-situ with a high-speed video microscope during testing, c) shows the cross-section dimensions of the FIB notch and d) the cross-section dimensions of the drilled hole. The measurements for both are given in µm.

The notches or holes were manufactured by drilling (ɸ 50 - 200 µm) and FIB milling (w = 10 – 90 µm) into the type of test bars shown in Figure 7. The FIB milling was done with a FEI Helios Nanolab dual focused beam system. The FIB was set to a voltage of 30 kV and a milling current of 21 nA was used. The pattern was defined with a diamond shape seen in Figure 8 and Figure 9 with a notch height typically of 5-10 µm.
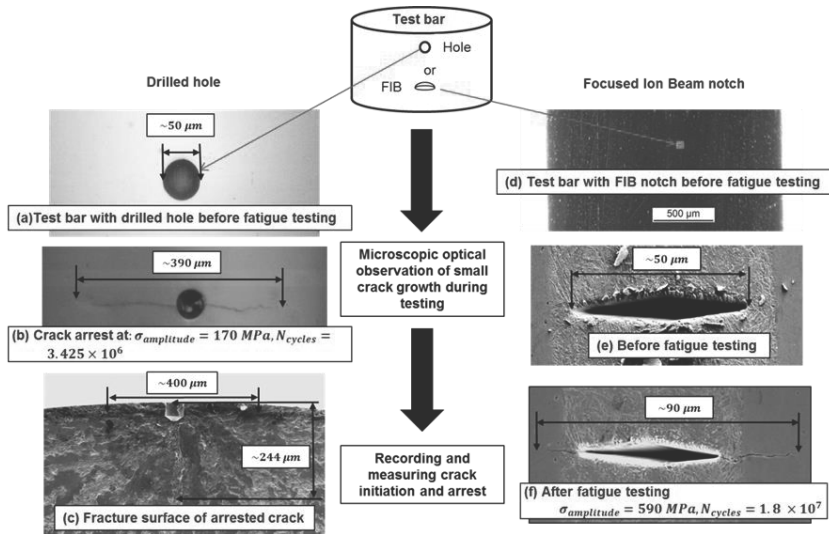
Figure 9. The test setup and method for measuring small crack growth from notches and holes. The parts (a) through (c) show the procedure used for drilled holes and (d) through (f) show the procedure used for FIB notches. A higher stress amplitude of 200 to 230 MPa was used to cause failure of the test bar and the fracture surface of the specimens shown in (c).

The small holes and notches were monitored optically during the testing to detect small crack initiation and growth. Once the test bar failed or the test was complete it was examined with SEM, laser and optical microscopes. Sometimes the test bars failed from some other location such as an inclusion. Then the initiation site was studied with a SEM and the type, size, and shape of the initiation site was recorded.

Two types of small crack growth fatigue tests were performed. One was constant amplitude loading and monitoring of the fatigue crack growth from a notch. This means that the crack initiation and growth from the notch or hole are constantly monitored and measured in-situ, while the loading of the test specimen is constant. These types of tests were done in publications (III)-(V)

The other type of test that is reported in publication (V) is where:

1. The loading was slowly decreased as the crack grows to measure the arrest threshold of the small crack. Once this is done and after the crack has arrested,
2. The compressive portion of the loading is increased, while the maximum tensile stress was held constant. In other words, the arrested crack experiences a decreasing mean stress along with the increasing stress amplitude, but a constant maximum stress. The test was continued in this way with steps of 20-50 MPa in mean stress and each step was applied for about 1 million cycles or until crack growth is detected.

3. After crack growth is detected the stress amplitude is kept constant and the mean stress was decreased with constant monitoring of crack growth until the crack arrest was again confirmed.

After the crack arrest, step 2 is repeated again until the crack growth is detected. This type of testing was done with a starting stress ratio of R = -1, and with a stress amplitude of 450 MPa. The same testing procedure was also performed with a starting stress ratio of R = -2, where the maximum stress was 350 MPa and the minimum stress was -700 MPa.

| Accelerating Voltage | Spot Size | Magnification | Detector | 12C0256 |
| 20 kV | 3,2 | 1500 x | SE | ——20 μm—— |

Figure 10. A SEM image of a 20 μm FIB notch milled into the side of a test bar after 50000 cycles of fatigue testing. Publication (III)

Calculation of stress intensity factors

The results are analysed and presented using the $\sqrt{\text{area}}$ for inclusions, and the surface crack length for small cracks as seen in Figure 10. The threshold for crack growth or initiation for the different sizes of inclusions was calculated by using equation (18) [28].

$$\Delta K_{th} = 0.65 \cdot \Delta \sigma \cdot \sqrt{\pi \sqrt{\text{area}}} \qquad (18)$$

The other type of measurement was observed during testing, either in-situ or during interrupted loading. These results are reported as crack lengths on the specimen surface. The length of the surface crack was used to calculate the stress intensity factor range for the FIB notch test bar by using equation (19).

$$\Delta K = 0.65 \cdot \Delta \sigma \cdot \sqrt{\pi a} \tag{19}$$

In equation (19) the variable '*a*' is from the observed crack length of '*2a*'. Any crack solution becomes arbitrary, because continuum fracture mechanics are no longer valid in the studied dimensions. The same shape factor (0.65) was applied in both equations. This shape factor value is arbitrarily selected within a wide range of values generally used in literature [80,81]. In geometrical terms this equals an aspect ratio of $\frac{a}{c} = \pi/2$, where c is crack depth of a semi-elliptical crack.

Using the crack length measured from the surface the positive portion of the stress intensity factor range was calculated with the following equation:

$$\Delta K_+ = Y \cdot \Delta \sigma_+ \cdot \sqrt{\pi a}, \tag{20}$$

which for the exception of one loading case reported is equal to:

$$K_{max} = Y \cdot \sigma_{max} \cdot \sqrt{\pi a}, \tag{21}$$

Where '*a*' is half of the total crack length and Y is the geometry correction factor. The $\Delta \sigma_+$ is the positive portion of the stress range applied to the crack and σ_{max} is the maximum stress applied to the crack. In this study for all loading ratios, where R is negative K_{max} is equal to ΔK_+.   In this study all the data except for one set of data (where R = 0.26), K_{max} and ΔK_+ are the same value, although they are of course different in the fact that one is the stress intensity range (ΔK_+) and the other is the maximum stress intensity (K_{max}). The goal here is not to specify which works better, but rather to study the effect of compressive stress and therefore both work for the purpose required here.

There are two main differences between the two types of notches used. The FIB notches are smaller and more crack like with a high stress concentration ($K_t > 7$) and abrupt stress gradient. The drilled holes are larger and more like the non-metallic inclusions located in the steel with a lower but wider stress gradient ($K_t \approx 2$), which affects a larger volume of the steel around the hole than the FIB notch, also relative to their size.

3.5 Microstructure and small crack growth

In publication (IV) Focused Ion Beam (FIB) milling was used to create cross-sections, after which FIB imaging is used to make ion channeling contrast pictures of the microstructure [67-70,72]. This imaging technique has been applied to small cracks in steels to study the profile in depth [68, 82]. Researchers have recently used the FIB tools to show how the size and crystal orientation of the grains affect the growth and direction of small cracks in the steel or other metalic materials [67,68,83]. In publication (IV) these tools and techniques are used to study the role that martensite sub-grain microstructure has on the initiation and growth of small fatigue cracks in high-strength steels from inclusions and notches.

The interaction of non-metallic inclusions with the microstrucure in a hard bearing steel (100Cr6) and a quenched and tempered steel (34CrNiMo6) is examined in publication (IV). The non-metallic inclusions found in the steel promote subsurface crack initiation. A new technique used in publication (IV) is Focused Ion Beam (FIB) milling to study the microstructure around an inclusion that has caused fatigue failure in the ultra-long fatigue life regieme. These FIB millied and imaged cross-sections of the inclusion and microstrucure are then compared with similar cross-sections of small cracks which have grown from FIB-milled semi-elliptical notches tested near the endurance limit of the steel. The crack path of the small cracks from the FIB notches are then be compared with the crack paths of small cracks from non-metallic inclusions that failed at or near the endurance limit.

4. Results

4.1 Fatigue testing

4.1.1 Rotating bending fatigue testing

A total of 61 rotating bending fatigue test bars were tested from the large forged steel roll (see publication (I)). There were 42 test bars that were tangential to the axis of the steel roll and 19 that were parallel to it. The reason a greater number of test bars was sampled from the tangential direction is because of the larger inclusions that were found there and the greater scatter in the fatigue test results. The results of the fatigue tests are shown in Figure 11.
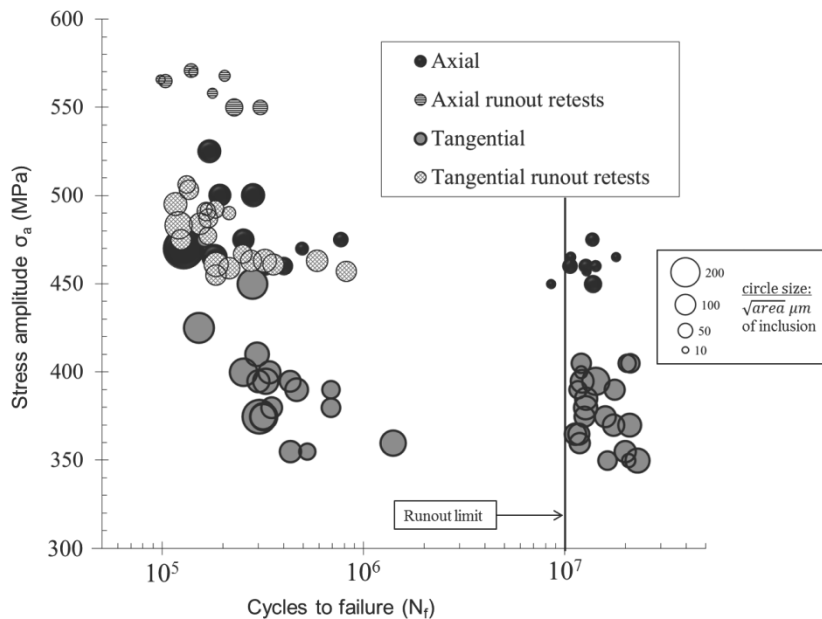

Figure 11. The results of the fatigue tests with cycles on the x-axis and the stress amplitude (MPa) on the y-axis. The circle sizes represent the size of the inclusion located at the site of fatigue crack initiation.

There was a significant difference between the two different directions from which the fatigue test bars were taken from the steel roll. The axial fatigue test bars displayed a significantly higher level of fatigue limit when compared to the tangential fatigue test bars.

4.2   Maximum likelihood analysis

The MML method of analyzing staircase fatigue test results is outlined in Ref. [38]. Using this method the fatigue limit of the tangential test bars was calculated to be 369.7 MPa, with a standard deviation of ± 35.6 MPa and the fatigue limit of the axial test bars was calculated to be 463.1 MPa, with a standard deviation of ± 11.2 MPa.

4.3   Binomial probability analysis

The binomial probability analysis method was applied to the fatigue test data. Using this method the average fatigue limit as well as the standard deviation of the strength was calculated for the tangential and axial test bars. The organization of the data along with the application of the binomial analysis method is shown in Table 3 for axial test bars and Table 4 for tangential test bars. The assumption that is made in the calculation of the amount of failed and runout test bars is that if the fatigue test at a certain stress level was a runout then the result would have been the same for all lower levels of stress. The opposite also applies when a failure occurs at a certain stress level and the test bar would have failed at all higher stress levels as well. The probabilities listed in these tables were calculated using equation (16). [39,40]

Table 3. Binomial probability analysis of axial test bars.

Stress (MPa)	Runout	Failed	ΣFailed/ΣRunout	$\Sigma F/\Sigma N_{total}$	P(5%)	P(50%)	P(95%)
450	1	1	1/8	1/9	3.70	16.20	39.40
457	1	0	1/7	1/8	4.10	18.00	42.90
460	3	2	3/6	3/9	15.00	35.50	60.70
465	2	1	4/3	4/7	28.90	56.00	80.70
470	0	2	6/1	6/7	52.90	79.90	95.40
475	1	2	8/1	8/9	60.60	83.80	96.30
500	0	2	10/0	10/10	76.10	93.80	99.50
525	0	1	11/0	11/11	77.90	94.30	99.50

Table 4. Binomial probability analysis of tangential test bars.

Stress (MPa)	Runout	Failed	ΣFailed/ ΣRunout	ΣF/ΣN$_{total}$	P(5%)	P(50%)	P(95%)
350	3	0	0/22	0/22	0.30	3.00	12.30
355	1	2	2/19	2/21	3.80	12.00	25.90
360	1	1	3/18	3/21	6.50	16.40	31.60
365	2	1	4/17	4/21	9.40	20.90	36.90
370	2	0	4/15	4/19	10.40	23.00	40.10
375	2	3	7/13	7/20	20.60	35.90	53.60
380	1	2	9/11	9/20	28.60	45.30	62.80
385	2	0	9/10	9/19	30.20	47.50	65.30
390	2	2	11/8	11/19	39.40	57.40	74.10
395	2	3	14/6	14/20	51.30	68.70	83.20
400	1	2	16/4	16/20	61.60	78.10	90.10
405	3	0	16/3	16/19	65.60	81.90	92.90
410	0	1	17/0	17/17	84.60	96.20	99.70
425	0	1	18/0	18/18	85.40	96.40	99.70
450	0	1	19/0	19/19	86.00	96.50	99.70
475	0	1	20/0	20/20	86.70	96.70	99.70

The fatigue limit of the tangential test bars calculated according to the binomial analysis is 386 MPa, with a standard deviation of ± 20 MPa, and for the axial test bars the fatigue limit is 463 MPa, with a standard deviation of ± 12 MPa.

In Figure 12 and Figure 13 the level of the estimated average fatigue limit (P(50%)) at 10^7 cycles is indicated by the intersection of the 50% failure probability red line and the 50% confidence blue line. The binomial analysis also gives the 95% and 5% confidence levels that are associated with each failure probability level.
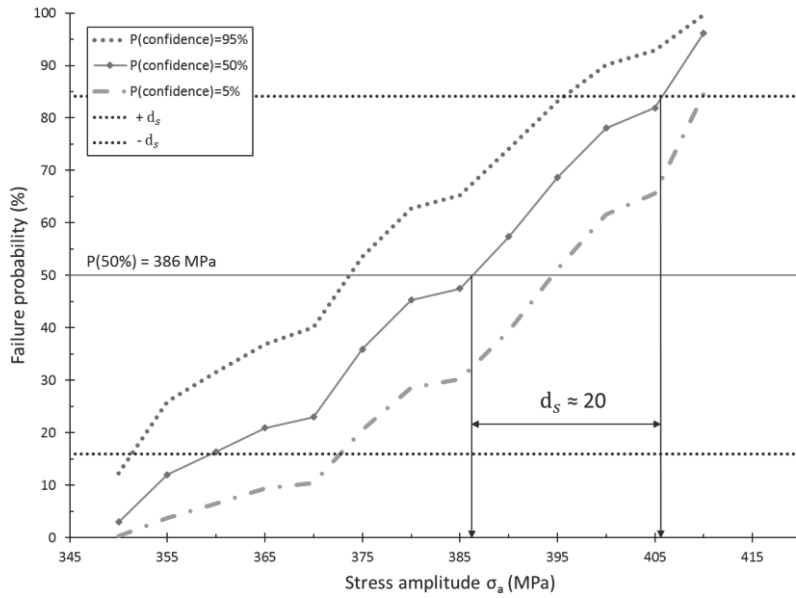
Figure 12. The results of the fatigue tests performed on the tangential test bars. The fatigue limit and standard deviation are calculated according to the binomial method. The black dotted lines indicate one standard deviation.
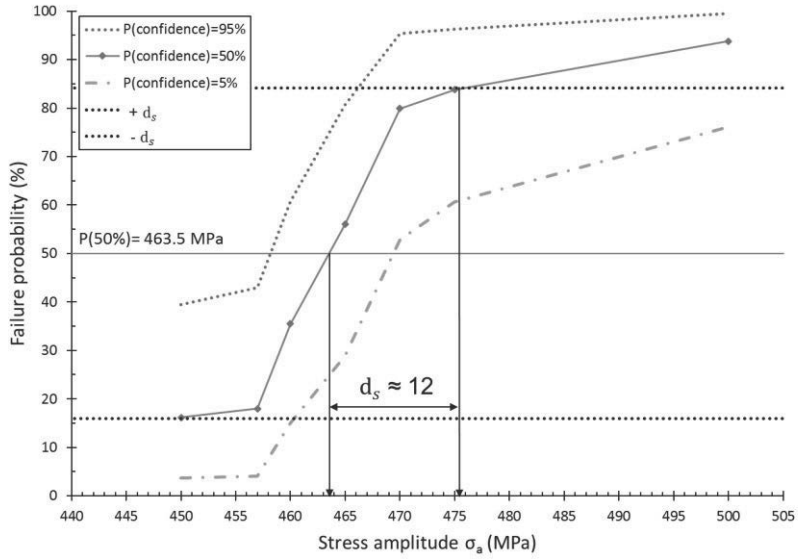
Figure 13. The results of the fatigue tests performed on the axial test bars. The fatigue limit and standard deviation are calculated according to the binomial method. The black dotted lines indicate one standard deviation.

The results of the two different analysis for the axial and tangential fatigue test bars are given in Table 5.

Table 5. The comparison of the two different methods used to calculate the fatigue limit and standard deviation from fatigue test results.

	Fatigue limit Axial (MPa)	Deviation Axial $\pm d_s$ (MPa)	Fatigue limit Tangential (MPa)	Deviation Tangential $\pm d_s$ (MPa)
MML Analysis	463.1	11.2	369.7	35.6
Binomial Analysis	463	12	386	20

4.3.1 Rotating bending fatigue and Murakami-Endo model

The use of equation (5) gives the lower bound fatigue limit considering that the maximum inclusion square root area is the largest in the specimen and that it is the cause of failure. The application of the Murakami-Endo model to the fatigue data is shown in Figure 14.
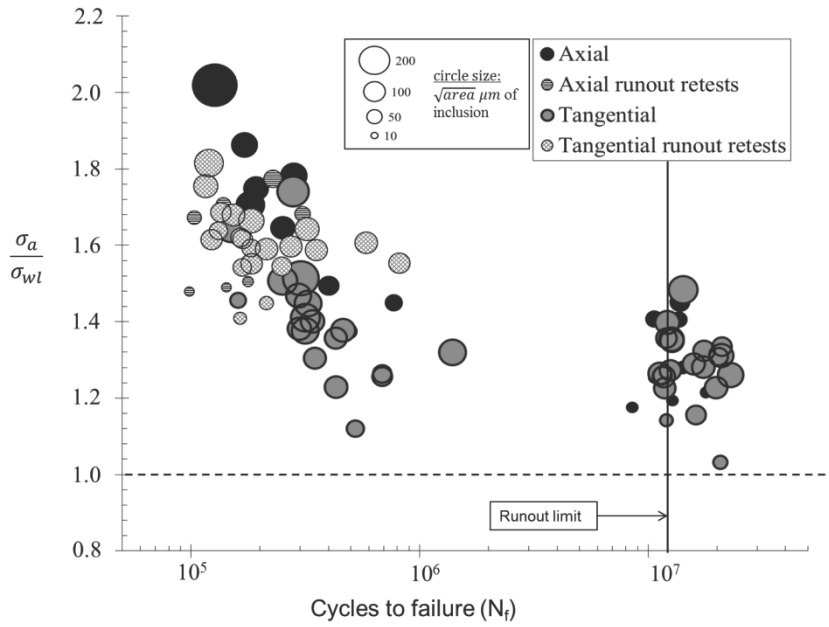
Figure 14. The application of the Murakami-Endo model to the fatigue test data.

4.3.1 Axial fatigue testing

The endurance limit at 10^7 cycles of the smooth un-notched test bars was determined at R = -1. The results of the fatigue testing are shown in Figure 15 (see publication (V)). The endurance limit was calculated to be 475 MPa ± 11 MPa by using the MML method described in Ref. [38].
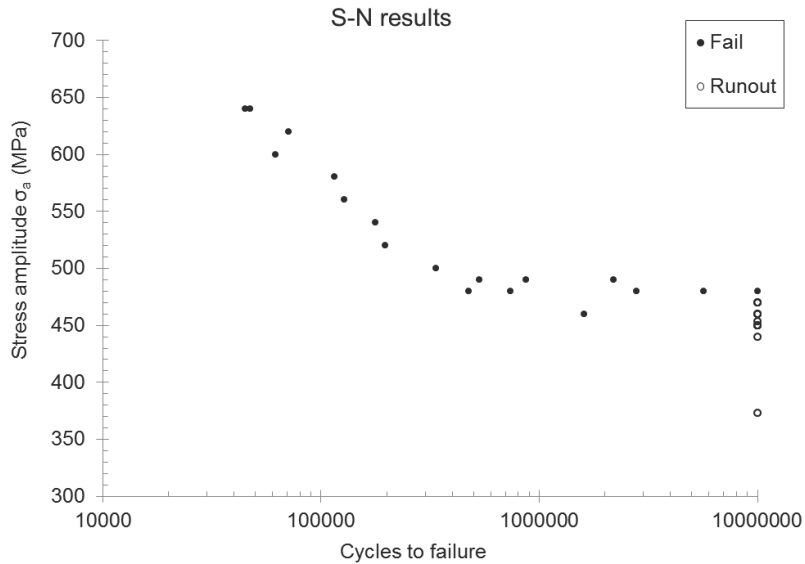
Figure 15. Fatigue stress - life curve and endurance limit determined for smooth bar specimens of the test material – quenched and tempered 34CrNiMo6(B) steel.

4.4   Inclusion analysis

4.4.1   Rotating bending fatigue and inclusion analysis

The results of the automated inspection of the polished specimens yielded a total of 11300 inclusions. A summary of the findings is presented in Table 6.

Table 6. The results of the INCA Feature inclusion analysis.

	Total number of in-clusions	Average size (μm^2)	Average aspect ratio
X-plane	3136	30.39	1.71
Y-plane	4812	21.5	1.63
Z-plane	3352	25.3	1.67
Total	11300	24.98	1.65

The calculation of the maximum inclusions found on the polished specimen was done by measuring the maximum length and width of the inclusion and then using the equation for the area of an ellipse, which is given as:

$$A = \pi \cdot \frac{(a \cdot b)}{4} \qquad \qquad (22)$$

where a is the length and b is the width of an ellipse that best describes the shape of the largest inclusion found on the control surface of the polished specimen. The same method was used for fracture surface inclusions using an ellipse that best describes the shape of the inclusion or cluster on the fracture surface. An example of a maximum inclusion on a polished specimen is shown in Figure 16 and the measurement of the size of the inclusion on a fracture surface is shown in Figure 18. The $\sqrt{area}$ of an inclusion for both polished specimen as well as fracture surface inclusions is calculated as the square root of A in equation (22).
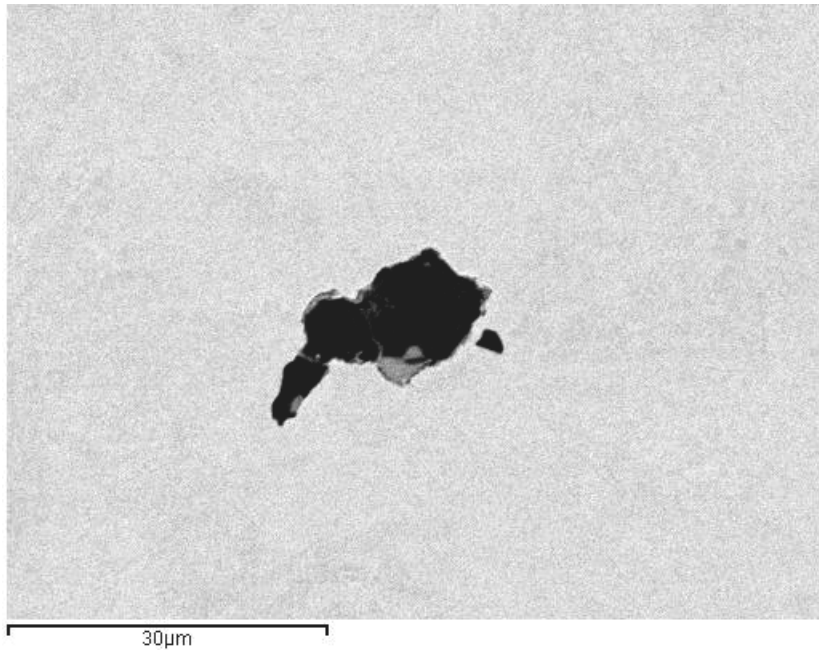

30µm

Figure 16. An example of a maximum inclusion found on a polished specimen.

The site of fatigue crack initiation on all except for three of the 61 fatigue test bars was an inclusion that was on or near the surface of the test bar. These three test bars that did not show evidence of inclusions at crack initiation sites were all from the axial test bar group and two of the three were runouts, with the third bar failing at 8 million cycles. The type of inclusions found at the site of crack initiation were mostly different types of aluminium oxides with the exception of 8 test bars, all of which were from the tangential group. In these test bars the fatigue cracks initiated from large inclusions composed of manganese sulfide. In Figure 17 is shown one of the MnS inclusions.
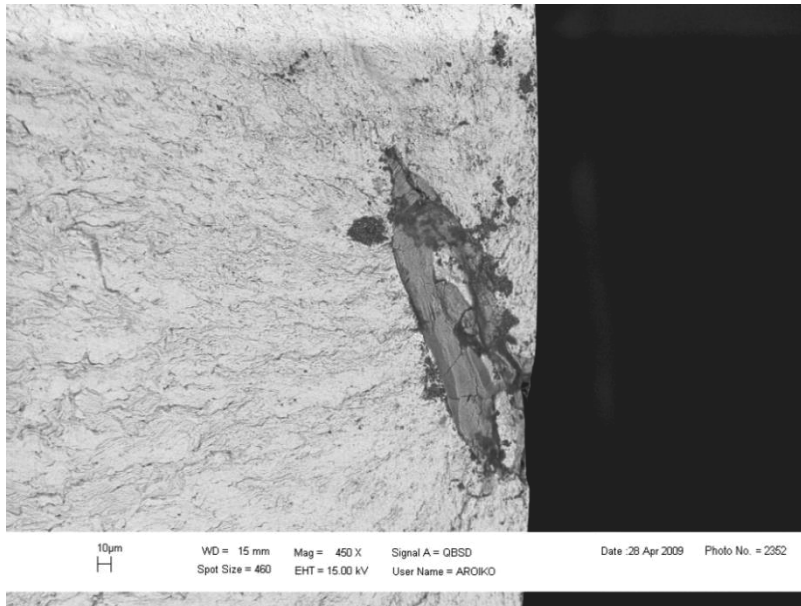
Figure 17. A manganese sulfide inclusion at the site of crack initiation on a test bar as an electron backscatter image.

Figure 18. An example of the measurement that was done to determine the size of the projected area for the inclusions that are found on the site of fatigue crack initiation.

Using the MML method to estimate the parameters of the Gumbel distribution from the inclusion data obtained from the fracture surface and polished specimen it is possible to calculate the estimated largest extreme value distribution (LEVD), as well as the upper and lower confidence levels. These extreme value probability plots for the fracture surface inclusions as well as polished specimen inclusions are shown in Figure 19 and 20.
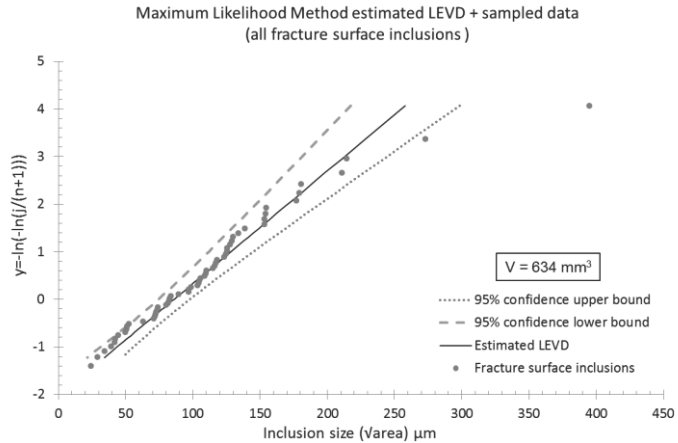

Figure 19. The extreme value probability graph of the largest inclusions from the fracture surface inclusions.
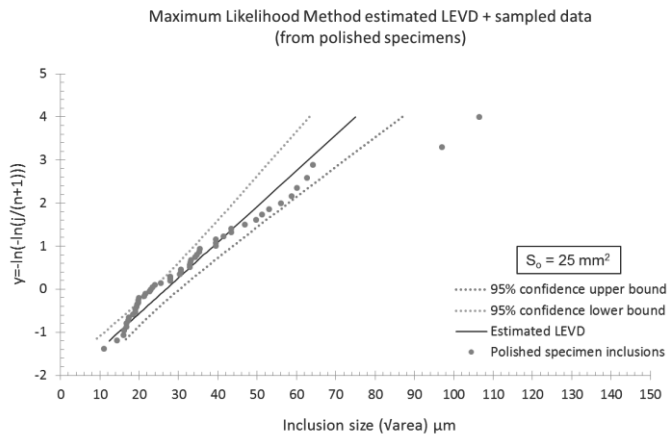

Figure 20. The extreme value probability graph of the largest inclusions from all the polished specimen maximum inclusions.

The comparison of the inclusion distribution within the various planes of the steel roll was done as well. The parameters and the average maximum inclusion size along with the standard deviation of these distributions are shown in Table 7. The differences in the extreme value distributions of the inclusions from the fracture surfaces compared to the polished specimens indicate that a larger inspection area is required.

Table 7. The average size of the inclusions in different positions of the test bars and polished specimens as well as their extreme value distribution parameters for the Gumbel distribution.

	Average Inclusion size (√area) μm $\bar{\lambda} = \lambda + \delta \cdot \gamma$	Standard Deviation Inclusion size (√area) μm $D_G = (\delta \cdot \pi)/\sqrt{6}$	Lambda (λ) Location Parameter Gumbel	Delta (δ) Scale Parameter Gumbel	Number of Inclusions Studied
All FS	110.42	54.25	86.0	42.3	58
All PS	33.78	15.52	26.8	12.1	54
Axial (Y)-FS	90.69	57.97	64.6	45.2	16
Axial (Y)-FS[1]	75.25	39.89	57.3	31.1	15
Tangential (X)-FS	115.42	49.38	93.2	38.5	42
Axial (Y)-PS	26.17	9.49	21.9	7.4	18
Tangential (X)-PS	45.43	22.96	35.1	17.9	18
Z-Plane (Z)-PS	29.45	11.67	24.2	9.1	18
Axial (Y)-FS (Ro)	43.72	16.03	36.5	12.5	6
Axial (Y)-FS (F)	121.62	68.49	90.8	53.4	10
Tangential (X)-FS (Ro)	101.32	38.48	84.0	30.0	16
Tangential (X)-FS (F)	137.15	58.10	111.0	45.3	19

[1] The calculation of parameters excluding the largest inclusion found on an axial test bar fracture surface that was exogenous in nature. FS = Fracture Surface, PS = Polished Specimen, Ro = Runout, F = Fail.

4.5 Small crack growth optical observation

4.5.1 Different types of notches compared to non-metallic inclusions

Data on crack initiation threshold was accumulated also through fractography of many specimens tested near the fatigue limit of the steel. A large set of test data for a different batch of the same steel type was available from a previous project

[84]. Results of five specimens in that set are used here for comparison. They exhibited crack initiation at an inclusion just breaking the specimen surface after more than 10 million fatigue cycles. This data is plotted in Figure 21, where a comparison can be made between different defects initiating a fatigue crack near the fatigue threshold.

The data used to calculate the stress intensity factor for the inclusion data points is the inclusion size and the stress level at which the test bar failed. The FIB data points are at the stress level at which the crack initiated and then arrested. Two of the drilled hole points represent crack initiation at the hole. Pre-cracking with compressive mean stress was introduced to one of them.
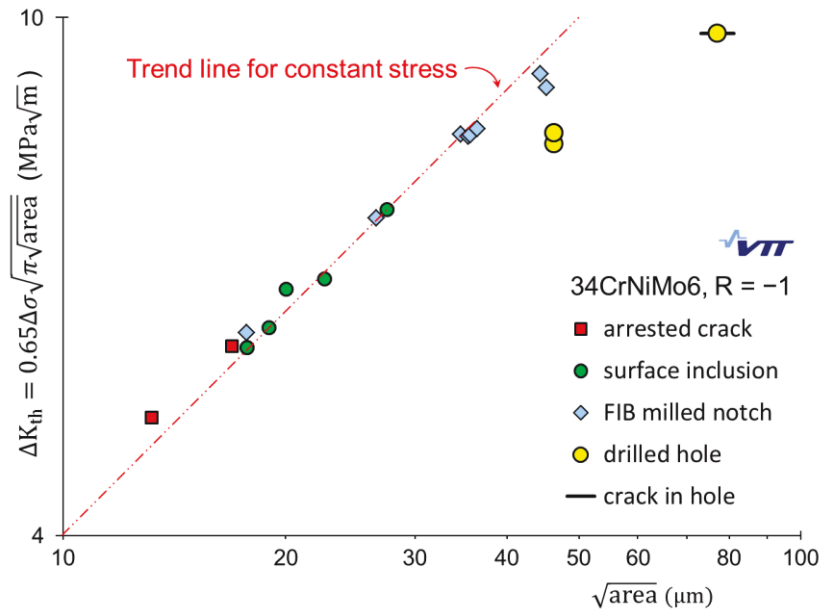

Figure 21. The stress intensity range vs. the square root area of the initiator at the growth threshold condition (≈ fatigue limit) for different types of notches.

The same data shown in Figure 21 is also plotted with respect to the stress amplitude of the fatigue test compared to the initiating defect size. This is shown in Figure 22, along with a trend line for constant stress amplitude.
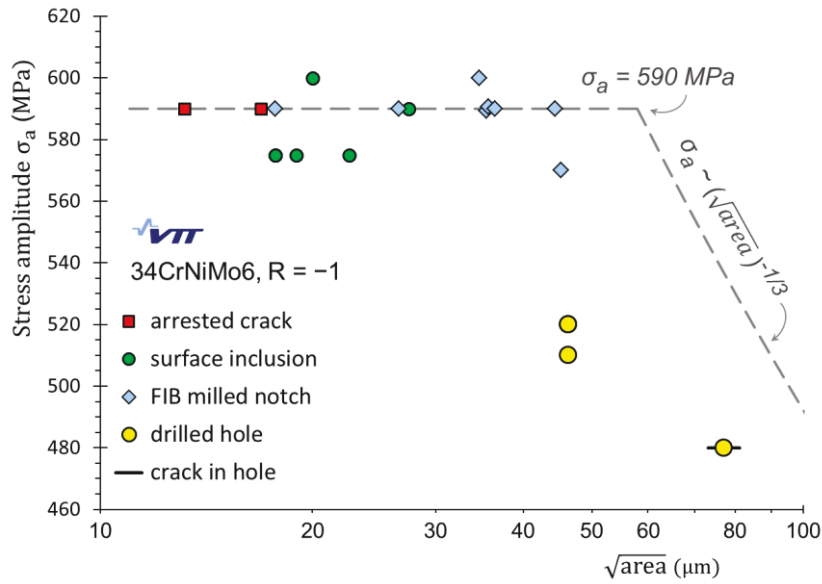
Figure 22. The same data as in Figure 21: fatigue limit as function of initiator size.

4.5.2   FIB notches for small crack growth

A test bar with 20 small FIB notches gave a large and interesting set of results, because crack growth was observed in almost all notches irrespective of their different sizes. The observed crack growth in 34CrNiMo6 QT(A) steel studied in publication (III) is shown in Figure 23.
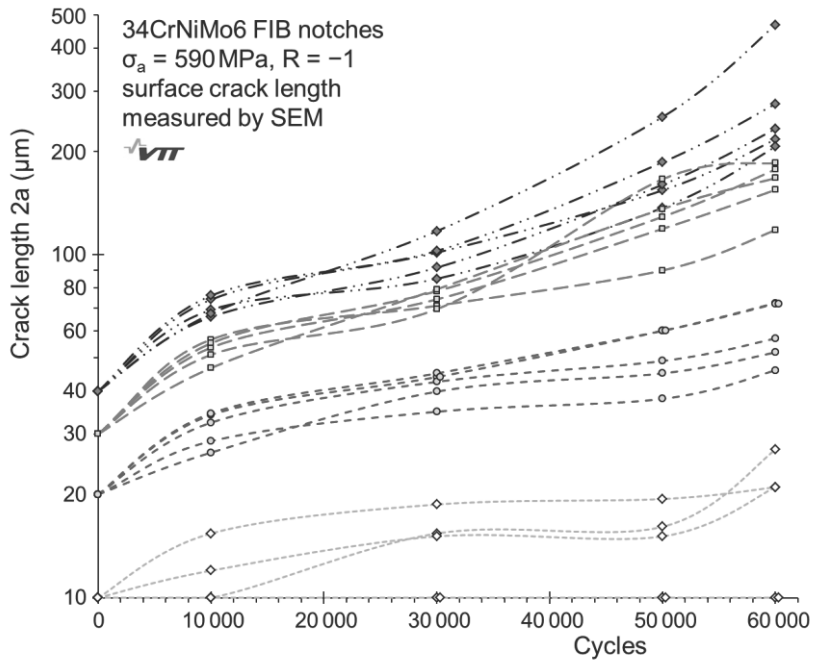
Figure 23. Growth of small cracks from 10, 20, 30 and 40 µm sized FIB-milled notches (5 of each) in a test bar of 34CrNiMo6 QT(A) steel.

The data in Figure 23 can be used to calculate the crack growth rate versus the stress intensity factor range. This was done by averaging the crack growth rate as well as the stress intensity factor range over each observation interval. These results are illustrated in Figure 24 where they are separated into original notch sizes. To illustrate the variation of growth rate along the cycle count, another grouping of the same data is also shown.
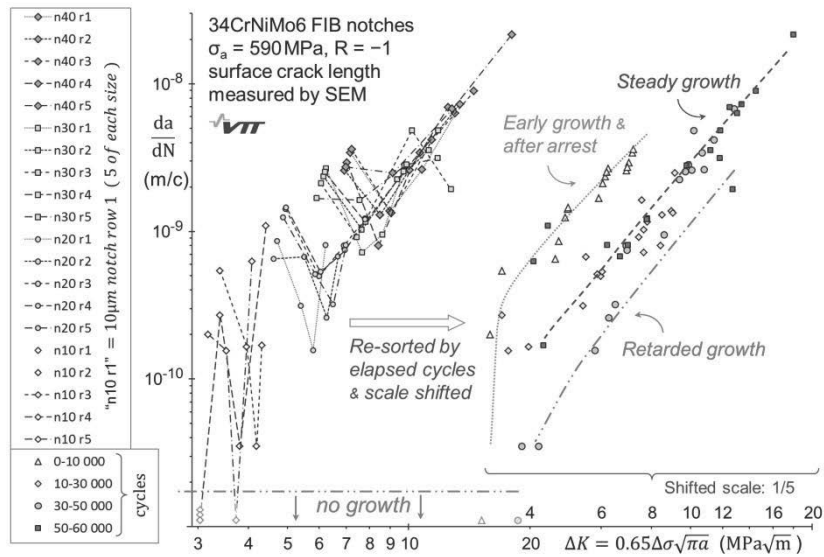
Figure 24. Crack growth rate curves based on data in Figure 23. On right the same data is sorted according to phase of test.

Crack growth from FIB notches was first studied with constant loading near the fatigue limit. This means that once the crack has initiated the test can be characterized as a rising ΔK test. Results from one such test from publication (VI) are shown in Figure 25.
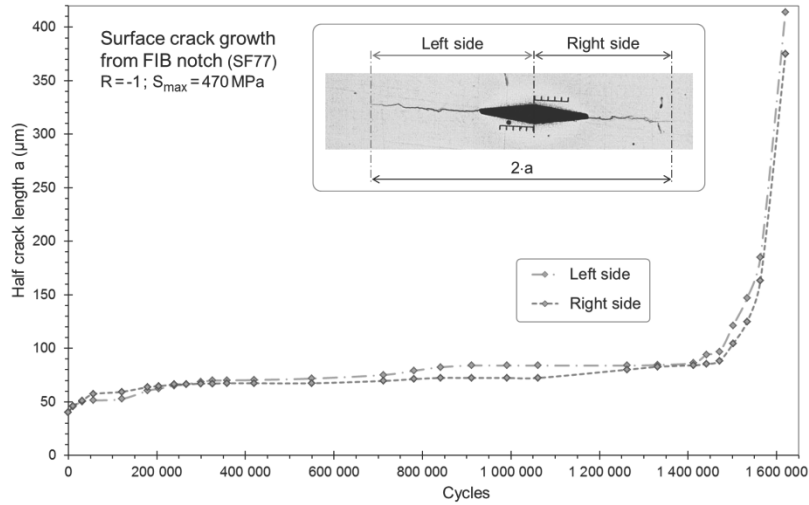
Figure 25. The results of in-situ optical measurements of crack growth from a FIB notch under constant amplitude loading. The x-axis is the number of fatigue cycles and the y-axis is the crack length on the left (red) and right (blue) side of the notch. These tests and the following test were done on 34CrNiMo6 QT(B) steel. S_{max} is the maximum value of the stress amplitude at which the fatigue test bar was loaded.

From Figure 25 it can be observed that the cracks initiate almost immediately and grow fast in the beginning of the test. Once the crack grows out of the area directly ahead of the notch where there is a stress gradient, the driving force decreases and the crack growth rate slows down. From around 50 000 cycles to around 1.4 million cycles there is a phase of slow, but constant and symmetric growth of the crack. This phase of slow growth leads the small crack out of the growth threshold region into the normal crack growth rate region for large cracks.

Using the data from Figure 25 and Equations (20) and (21) we can calculate the da/dN vs ΔK_+ or K_{max} correlation which is shown in Figure 26.
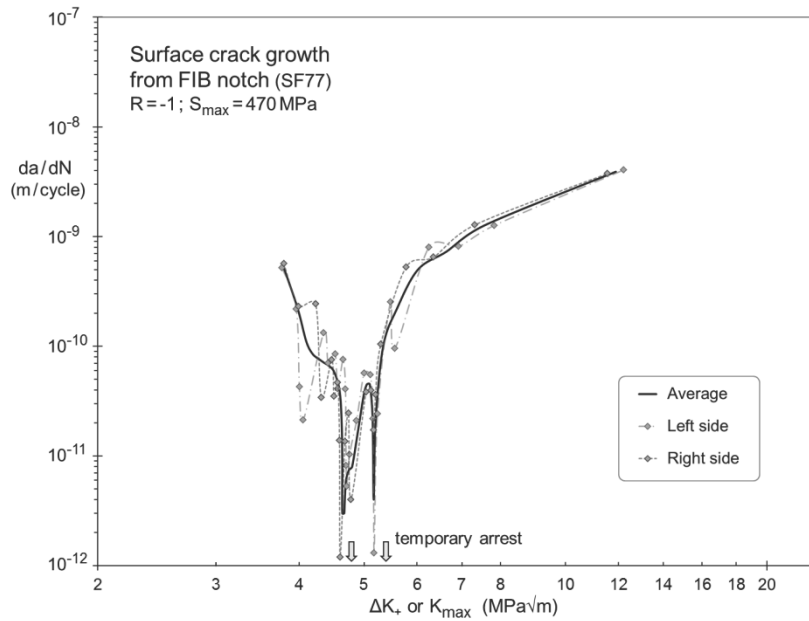
Figure 26. The crack growth data from Figure 25 is used to calculate the da/dN vs. ΔK_+ or K_{max} graph showing the crack growth rate from the FIB notch. S_{max} is the maximum value of the stress amplitude at which the fatigue test bar was loaded.

Figure 26 illustrates that in the slow growth region the crack is growing slower than the rate for determining the growth threshold (da/dN < 10^{-10} m/cycle) and the data shows a decreasing crack growth rate. This is because of the large increase in the fatigue cycles compared to the actual crack growth. What is also important to observe is that the crack is actually growing for most of the time, at least on the surface. This data shows that the small crack growth rate behaviour is a slow process that gradually approaches the threshold of crack growth for large cracks.

4.5.3   Small crack growth and loading

The averaged curve in Figure 26 is repeated together with the other test results obtained using FIB notches at different R-ratios. This compilation is shown in Figure 27.
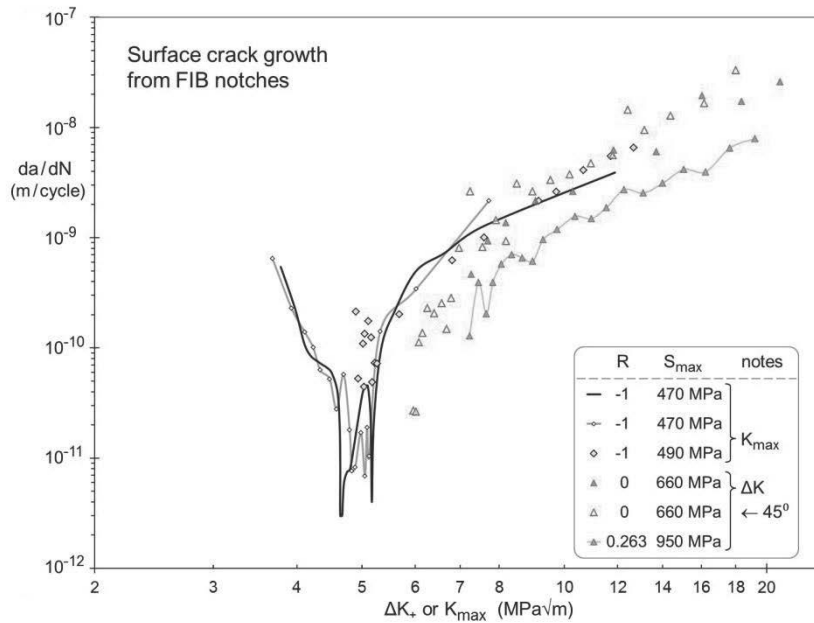
Figure 27. The initiation and growth of small cracks from FIB notches at different R-ratios. All results shown here are from test bars made with 34CrNiMo6 QT(B) steel. S_{max} is the maximum value of the stress amplitude at which the fatigue test bar was loaded. One data set marked 45° is a FIB notch that was milled at 45 degrees to the loading direction.

Once the positive portion of the stress intensity factor range (ΔK_+) is greater than 5 MPa$\sqrt{m}$, the crack grows out of the threshold zone into the conventional crack growth rate stage II of the Paris law curve.

4.5.4   Small drilled holes for small crack growth

The other type of small notch used was drilled holes. The crack growth rate from drilled holes during constant amplitude loading is shown in Figure 28.
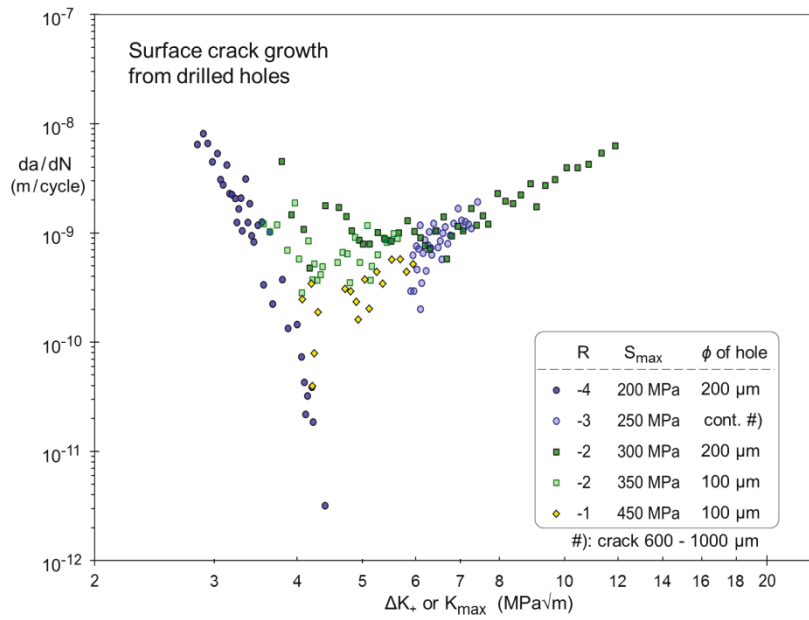
Figure 28. Growth rates of small cracks initiated from drilled holes at different R-ratios. All results shown here are from test bars made with 34CrNiMo6 QT(B) steel. S_{max} is the maximum value of the stress amplitude at which the fatigue test bar was loaded.

The constant amplitude crack growth rate data from the drilled holes and FIB notches are combined in Figure 29.
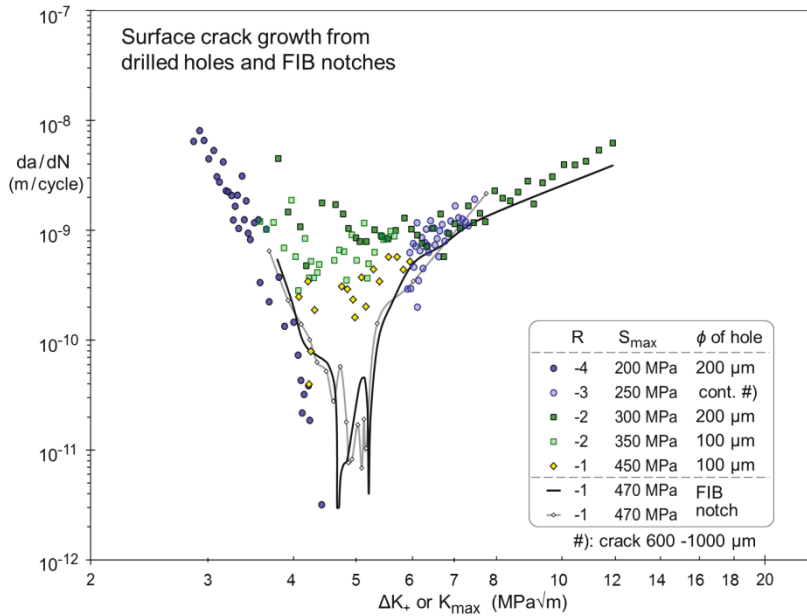
Figure 29. Growth rates of small cracks from drilled holes and FIB notches at different R-ratios. All results shown here are from test bars made with 34CrNiMo6 QT(B) steel. S_{max} is the maximum value of the stress amplitude at which the fatigue test bar was loaded.

The main difference with the crack growth rate from the drilled holes is that the crack growth rate is generally more stable and there is not as much crack growth rate deceleration as with the crack growth rate from FIB notches. This is due to the fact that the drilled holes have a stress gradient that decays gradually, whereas the FIB notches have stress gradients that are more crack like, so they are more severe, but affect a shorter distance.

When we combine the two data sets it can be seen that the drilled holes show a consistently higher crack growth rate and do not exhibit the same form of crack arrest with one exception of the crack that arrested under a R = -4 loading ratio. Total length of this crack was over 500 µm, when the growth rate became less than 10^{-10} m/cycle and over 600 µm at arrest. In other words, it was growing out of the stress gradient of the 200 µm hole during the decreasing rate phase. This means that the crack growth was greatly assisted by the compression portion of the loading as long as the crack tip was within the stress gradient of the hole. As the crack grew out of the stress gradient it gradually arrested.

The data in Figure 29 shows that using the positive portion of ΔK collapses the crack growth rate curves into the same curve for higher ΔK$_+$ regions. There is more scatter in the lower ΔK$_+$ regime due to the different nature of the notches, if they are drilled holes or FIB notches, and there is a larger influence of the microstructure that should be taken into consideration as well. However, once the cracks have grown out of the stress gradient they follow the same curve for the positive portion of the ΔK loading of the test material.

4.5.5   Effect of compressive loading on the threshold for crack growth

The other type of testing where the loading was controlled according to the growth of the crack from the drilled holes sheds light on the interaction between the compressive loading and small crack growth rate behaviour for different loading ratios. In this case the crack arrest was measured at a constant R-ratio of R = -1 and R = -2 and the results are shown in Figure 30.
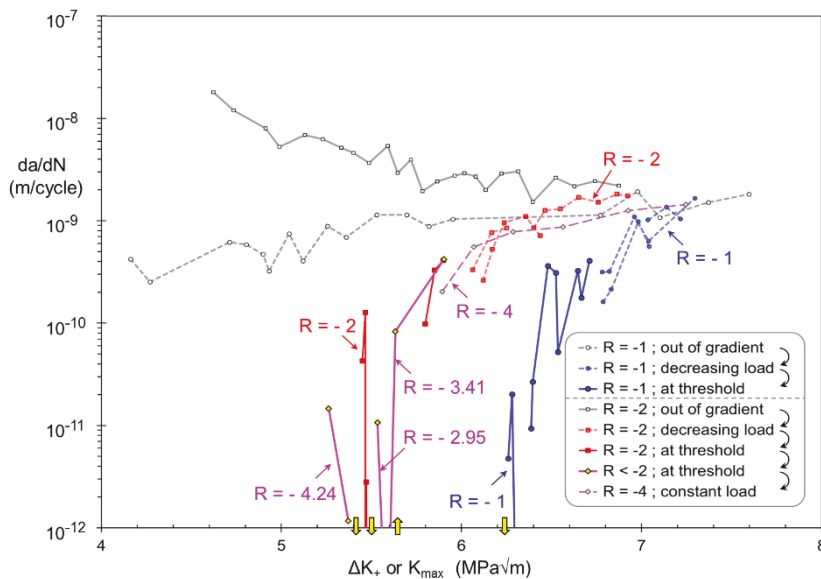
Figure 30. The initiation and growth as well as arrest threshold with decreasing ΔK (MPa√m). The grey lines are the original crack growth rate from the holes out of the stress gradient. After this the coloured data shows the arrest of the small cracks growing from small drilled holes as the stress amplitude is gradually decreased until the cracks have arrested. The blue data points and the blue lines are for the R = -1 loading and the red data points and the red lines for the R = -2 loading. The purple lines have the loading ratio assigned with an arrow showing the increased compressive portion of the loading. All results shown here are from test bars made with 34CrNiMo6 QT(B) steel.

It is clear from Figure 30 that under R = -2 loading the crack is growing at a faster rate than the crack under R = -1 loading, for comparable ΔK_+ or K_{max} values. When the two arrest thresholds are compared we see that the R = -2 threshold is about 12 % lower than the R = -1 threshold on the ΔK_+ or K_{max} scale.

The previous studies [53-55] about the effects of compressive loading on fatigue crack growth can be seen to apply also for small cracks in the steel that was studied here. It was measured that increasing the compressive loading for a crack can reinitiate its growth. This is due to the fact that increasing the compressive portion of the loading in constant amplitude testing decreases the ΔK_+ or K_{max} threshold for crack growth. The experimental work reported here is unique due to the new tools and methods that were employed to monitor and measure small fatigue crack growth under these unique conditions. For this reason there are almost no comparable data that could be used for comparison of the results reported in this study.

Figure 31. The comparison of the crack growth rates with the growth rate of small cracks loaded at R = 0. The average crack growth rate of small cracks loaded at R = 0 is shown with the dotted blue lines. All results shown here are from test bars made with 34CrNiMo6 QT(B) steel. S_{max} is the maximum value of the stress amplitude.

Figure 31 shows the difference between small crack growth rate at different R-ratios. The data shows that the average crack growth rate at R = 0 is in line with the crack growth rate at negative R-ratios and that there is a good correlation when using the positive portion of the stress intensity range once the crack has grown out

of the stress gradient of the hole. The interaction of the stress gradient from the hole and the crack growth rate is shown in Figure 32.
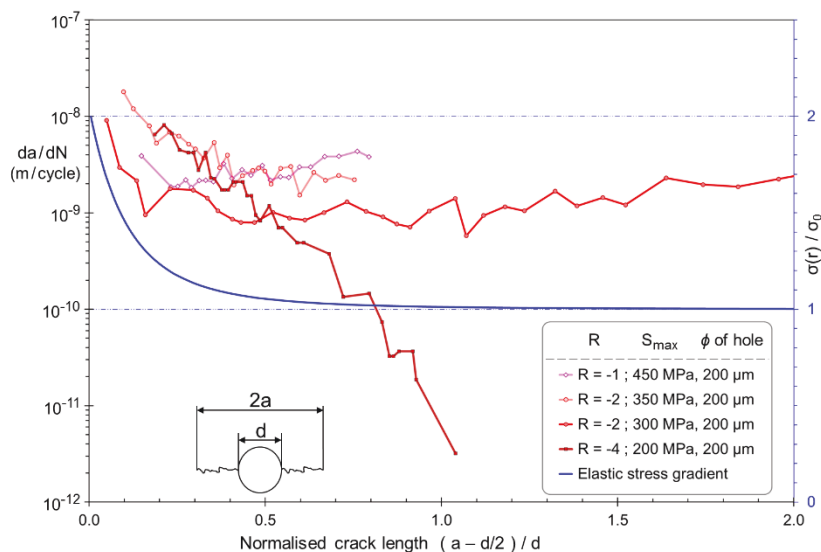
Figure 32. The change in the rate of crack growth from the hole with the crack length normalized to the diameter of the drilled hole. The legend gives the loading ratio R, after which is S_{max} which is the maximum value of the stress amplitude, and then the diameter of the drilled hole. The stress gradient for the drilled hole is given with the blue line which corresponds to the blue axis on the right side of the figure. All results shown here are from test bars made with 34CrNiMo6 QT(B) steel.

To obtain a better understanding of the behaviour of small crack growth rate under different negative R-ratios, the average crack growth rates were calculated for different portions of the crack growth test. This was done for crack growth measured at R = -2 to R = -3.73. This crack growth data is shown in Figure 33.
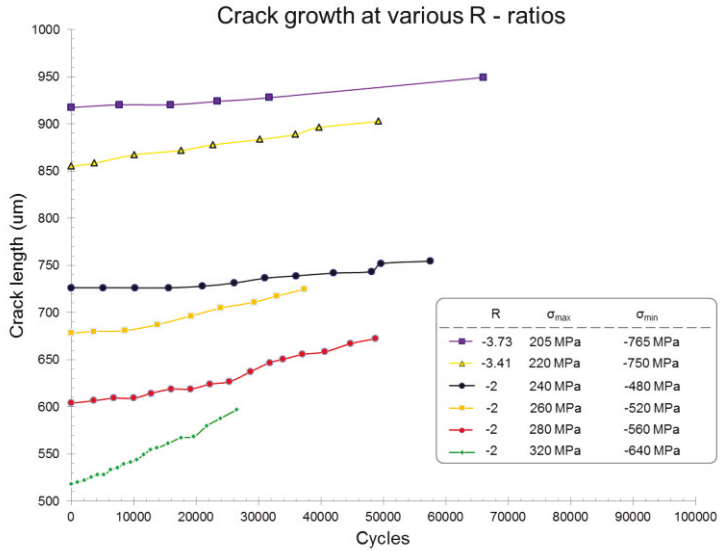
Figure 33. The crack growth measured during testing at different R-ratios. The maximum and minimum stress of the stress amplitude is given for the crack growth measured during 25000 to 70000 cycles of fatigue loading. All results shown here are from test bars made with 34CrNiMo6 QT(B) steel.

In Figure 33 the crack growth is shown for R-ratios -2 to -3.73. This data shows that generally the crack growth rate is linear for conditions where there is a large negative loading ratio. This data can be used to average the crack growth rate over a longer cycle count. Doing this a better overall picture is obtained of how the crack growth rate is behaving and eliminates some of the scatter caused by e.g. microstructural heterogeneity. The average crack growth rate data is shown in Figure 34.

Figure 34. The effect of different loading ratios on crack growth rate with respect to ΔK_+ or K_{max}. All results shown here are from test bars made with 34CrNiMo6 QT(B) steel.

Figure 34 shows that as the compressive loading portion of the fatigue cycle increases, the ΔK_+ or K_{max} at which a selected crack growth rate occurs decreases. When comparing the K_{max} for R = -1 and R = 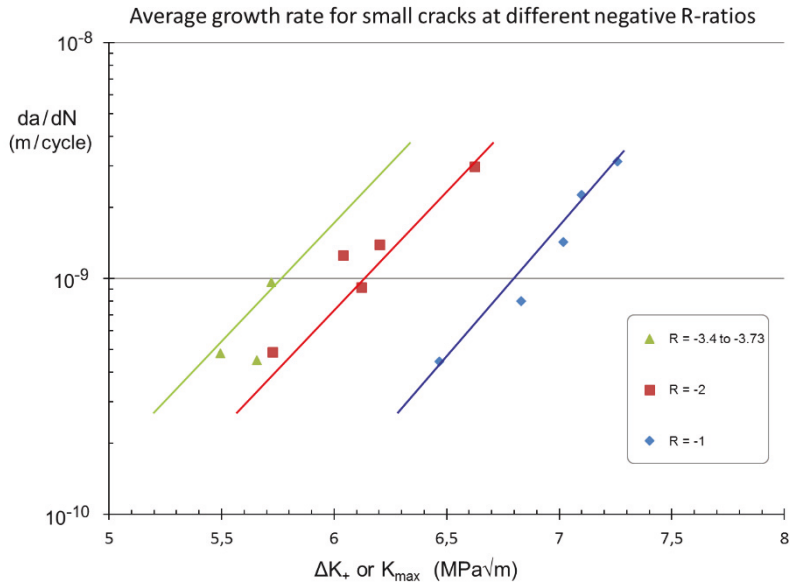-2, the decrease of similar effective ΔK_+ or K_{max} is around 12%, and there is around 7% decrease from R = -2 to R = -3.4 and -3.73. So it appears that there is a gradual saturation for the effect of the amount of compressive loading on the correlation between the crack growth rate and ΔK_+ or K_{max}.

4.6   Fractography and FIB cross-sections

4.6.1   Crack paths in quenched and tempered 34CrNiMo6 QT steel – notches on the surface

Using FIB notches as initiation points for small cracks, it is possible to mill the small cracks with the FIB as well as take ion images that reveal the local direction and flow of the microstructure. The crack shown in Figure 35 has been milled and imaged with a FIB and shows a small fatigue crack growing from a FIB notch along with the grain structure of the steel underneath the surface of the test specimen. In Figure 35 both (b) and (c) show how the location of the change in crack direction

corresponds to a change in the general martensite lath or packet direction. The paths of the small cracks that grew from the FIB notches show a clear preference in growth direction along the martensite packets or laths in the prior austenite grains. Once the crack grew through one prior austenite grain it changed direction and grew along the orientation of the martensite laths in the next prior austenite grain or martensite packet.
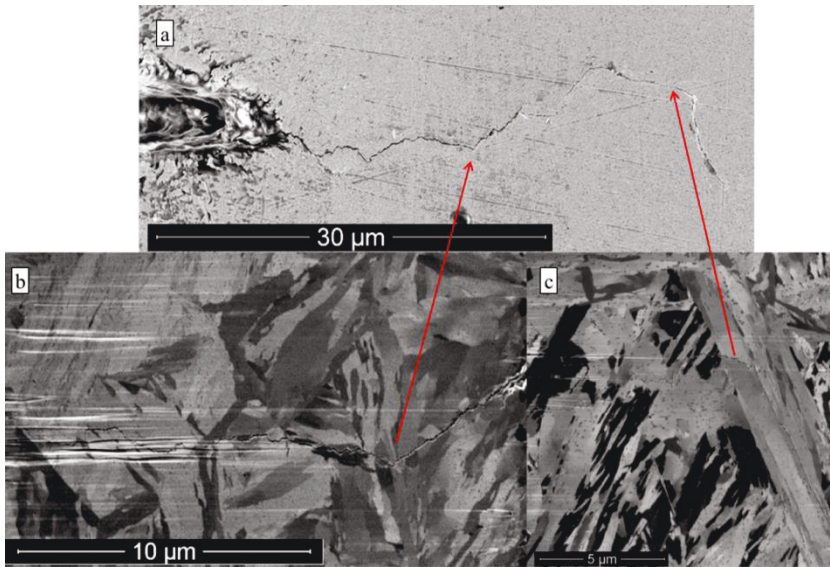
Figure 35. A small crack growing from a FIB notch (a) with two turning points correlated with the sub-grain microstructure (b, c). The stress ratio was R = -1 and the stress amplitude was 590 MPa. The test bar has been tested for 60000 cycles and was made of 34CrNiMo6 QT(A) steel. The remote stress is acting from top to bottom of the image.

The crack is propagating in a three-dimensional microstructure and the milling and imaging only shows a two dimensional structure, so it does not always follow exactly the specific martensite features. There is a noticeable change in direction at clear points where the martensite microstructure also changes. This is shown in Figure 35(c) where the crack turns abruptly away from the path that it was traveling and follows a large martensite packet or lath that is orientated in the same direction. This demonstrates that the local orientation of the microstructure has a definite influence on the growth direction of the small fatigue crack tested near the fatigue endurance limit.

Figure 35 and other similar images from publication (IV) show how the growth of small cracks from notches is greatly affected by the local sub-grain microstructure,

namely the orientation and size of the martensite microstructure along the path of the crack.

4.6.2   Crack paths in 34CrNiMo6 QT steel – subsurface inclusions and ODA

To study the microstructure and its eventual effects on crack growth from a non-metallic inclusion a long-life specimen was studied by cross-sectioning the initiation site. First we introduce some reference observations, and in particular, the fractographic feature "Optically Dark Area" (ODA) as defined by Murakami [6]. A comparison of observations on the same fracture surface by using different imaging techniques can be found in Ref. [20]. The images show an area of the fracture surface directly next to the inclusion that has an observably different topography than the rest of the surrounding fracture surface.

A smooth 34CrNiMo6 QT steel test bar was tested for $100 \cdot 10^6$ cycles at a stress amplitude of 550 MPa with an R-ratio of -1. The stress amplitude was then raised to 575 MPa and after $1.7 \cdot 10^6$ cycles at this stress amplitude the specimen failed. SEM images of the inclusion that caused the failure are shown in Figure 36 - 40. The area corresponding to the definition of "ODA" is marked besides the inclusion.
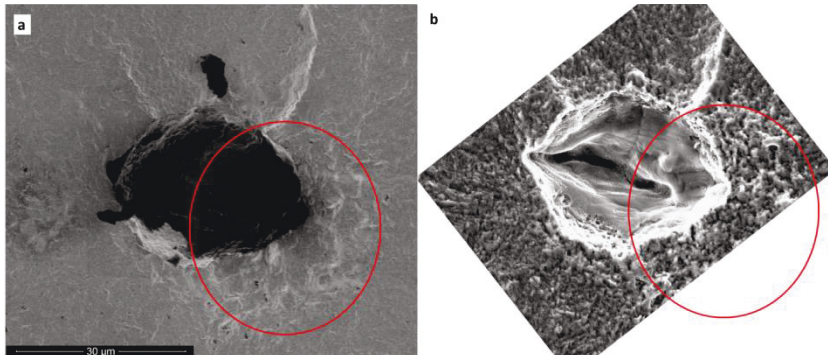
Figure 36. The non-metallic inclusion that caused failure in a smooth test bar. Picture (a) is an ion image taken with a FIB, and picture (b) is taken of the opposite fracture surface with a SEM microscope. Picture (b) has been flipped for easier comparison to picture (a). Both pictures have the same ODA area circled. The stress ratio was R = -1 and the stress amplitude was 550 MPa. The test bar has been tested for $100 \cdot 10^6$ cycles after which the stress level was raised to 575 MPa and the specimen failed after $1.7 \cdot 10^6$ cycles.   This specimen was made of 34CrNiMo6 QT(A) steel.

The two images in Figure 36 show the opposing sides of the fracture surface obtained by different types of microscopy. Figure 36(a) shows the fracture surface with

the inclusion in an ion image, and the conventional SEM image in Figure 36(b) shows the respective site on the opposite surface. Figure 36(b) has been flipped and rotated so that it is easier to compare with the fracture surface in Figure 36(a). The length scale is the same for both images.
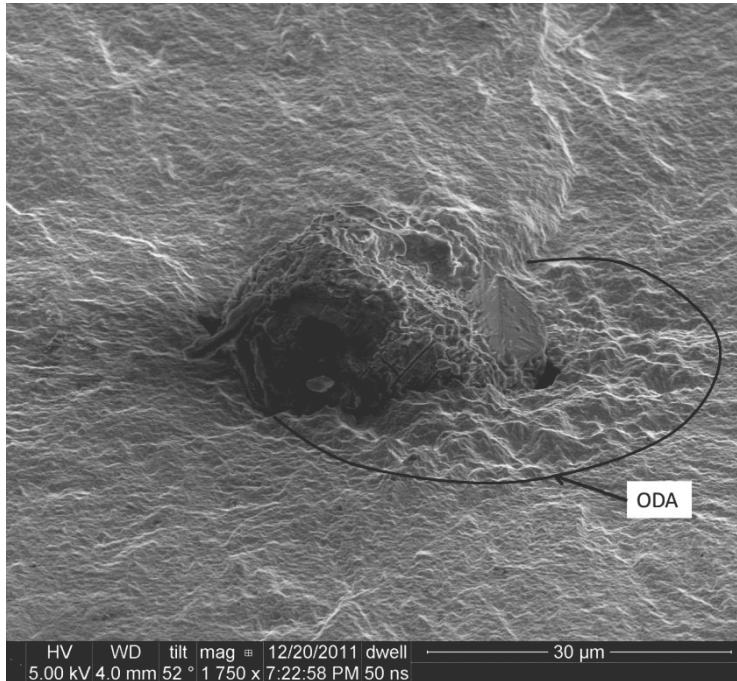
Figure 37. The non-metallic inclusion that caused failure in a smooth test bar. The part of the fracture surface circled by a black line is the ODA. This SEM picture was taken at an angle for a better topographic feature contrast. This specimen was made of 34CrNiMo6 QT(A) steel.

The inclusion and crack paths besides it were cut by FIB to see the microstructure below the fracture surface. The resulting cross-section is shown in Figure 38 and the images of the metal matrix on different sides of the inclusion are compared in Figure 39.
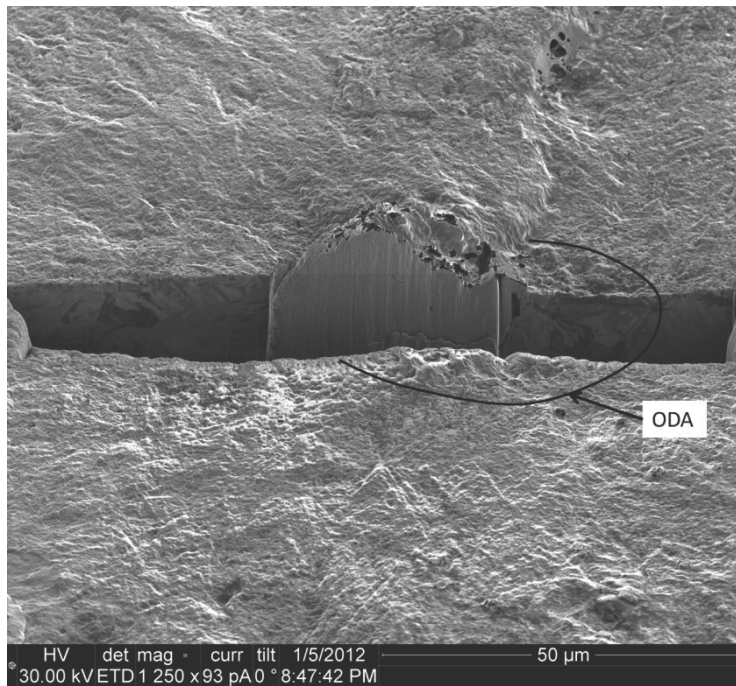
Figure 38. The cross-section FIB image of the ODA side and no ODA side of the non-metallic inclusion. This specimen was made of 34CrNiMo6 QT(A) steel.
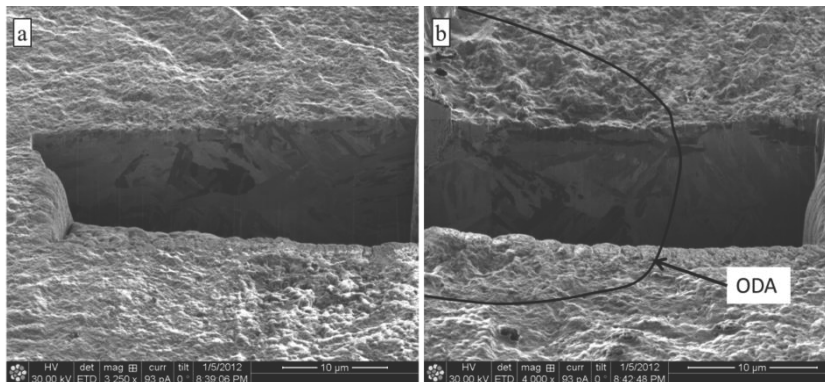
Figure 39. A comparison of the two cross-sections around the inclusion where (a) is from the side where there is no ODA and (b) is from the side where there is an ODA. This specimen was made of 34CrNiMo6 QT(A) steel.

In Figure 39(b) we can observe local martensite structure near and adjacent to the surface located inside the ODA area. This local microstructure is orientated in the same direction as the crack growth. By comparison in Figure 39(a), which is outside

of the ODA area on the other side of the non-metallic inclusion, it can be seen that the microstructural features are smaller and not orientated as preferentially to the direction of crack growth as the microstructure in Figure 39(b). This supports the connection between small crack growth and the size, shape and orientation of the microstructure and provides more information about the ODA area. It indicates that the formation of the ODA is connected to the initiation and growth of the small crack into the most preferential local microstructure surrounding the non-metallic inclusion.

4.6.3 Crack paths in 100Cr6 bearing steel – subsurface inclusions and ODA

A unique set of eleven 100Cr6 bearing steel test bars was tested at a common stress amplitude of 735 MPa at stress ratio R = -1 [19]. All specimens failed after high numbers of cycles ($N_f > 10^7$) from subsurface spherical oxides as shown in Figure 40.
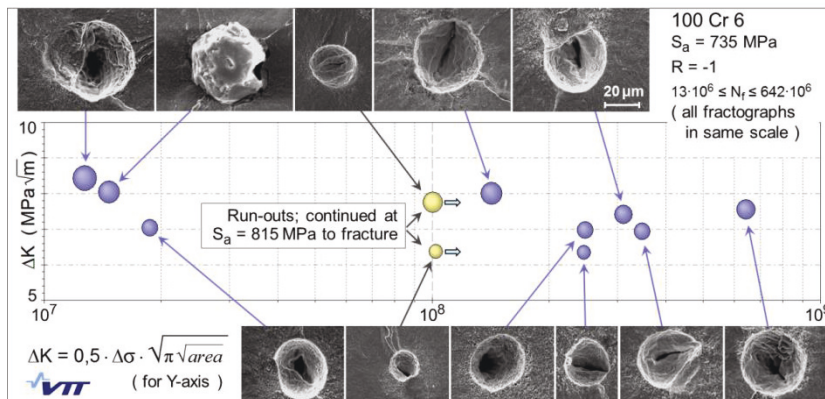
Figure 40. Fatigue initiators in 100Cr6 bearing steel. Sizes of balls indicate √area of inclusion. [19]

In Figure 40 can be seen a slight downward trend in the size of the crack initiating inclusion that correlates with an increase in fatigue life, but this correlation is not perfect. Some degree of scatter is inevitably expected in the UHCF regime, but we wished to take a closer look on crack initiation and growth paths over $10 \cdot 10^6$ cycles. In the following we focus on the test bar that gave the longest fatigue life of $642 \cdot 10^6$ cycles. Figure 41 shows the fracture surface around the inclusion, which was not the smallest in this set of specimens. Furthermore, the inclusion was located relatively close to the specimen surface, which is seen on top of Figure 41.

As shown in Figure 41, there are at least three crack initiation sites around the inclusion. Crack 1 occupies more than half of the inclusion circumference and has advanced the longest until the fish eye pattern is created by propagation of the crack to the specimen surface. Crack 3 lies on clearly different plane and has grown below cracks 1 and 2, thus causing retardation and unsymmetrical crack growth. It is worth of noting how long the ridges between the cracks reach. This demonstrates that the retardation effect has continued even beyond the crack sizes marked by the fish eye until the adjacent cracks have coalesced. We consider the rough surface besides the inclusion and in direction of crack 1 – opposite to crack 3 – as ODA. There seems to be a small area of ODA also within the crack 2.
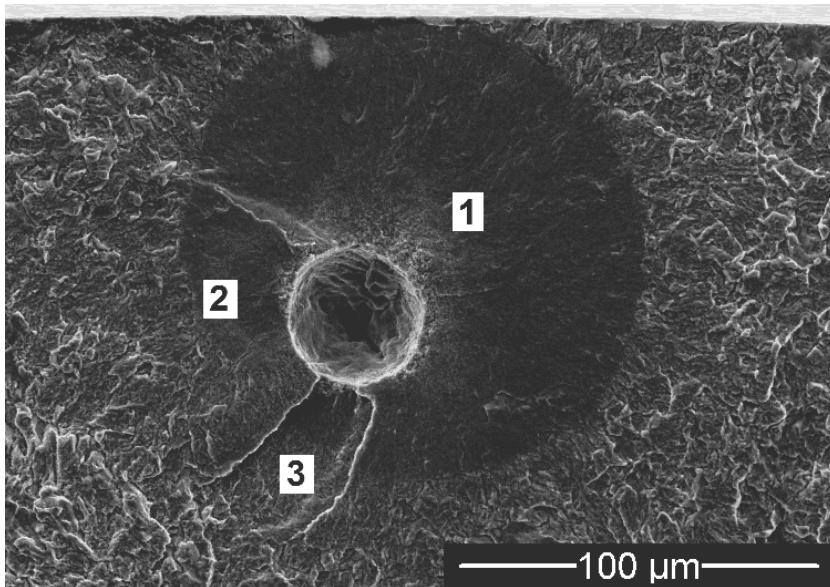
Figure 41. Crack paths around the inclusion associated with the longest endurance of 100Cr6 bearing steel. The stress ratio was R = -1 and the stress amplitude was 735 MPa. The test bar had been tested for $642 \cdot 10^6$ cycles.

The microstructure immediately below the fracture surface around the inclusion was studied. Two milled cross-sections were done (see Figure 42). The angled view clearly shows the long and about constant height of the step between the cracks 1 and 3. Once the first milled section was complete the surface of the cross-section was polished and then imaged with ions at a low current. The overview of the first cross-section with a comparison to the fracture surface is shown in Figure 42.

The left side of the first milled section shows the cross-section of the main ODA area next to the inclusion as well as the microstructure underneath the step between

the crack levels labelled '1' and '2' in Figure 41. The orientation difference revealed by the clear contrast in the underlying microstructure gives us a good reason to locate the two areas '1' and '2' in different prior austenite grains.
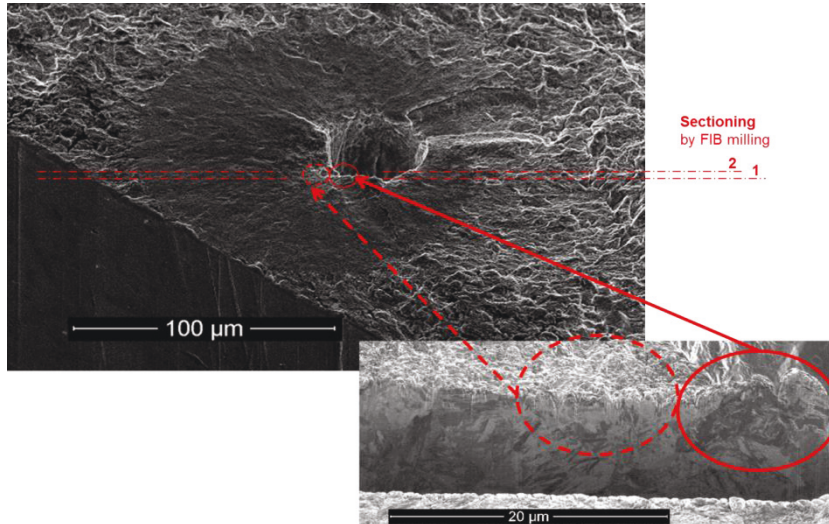
Figure 42. Comparing the microstructure of the step or ridge portion between crack levels '1' and '2' (see Figure 41) circled with a solid line and the microstructure of the ODA area circled with a dotted line.
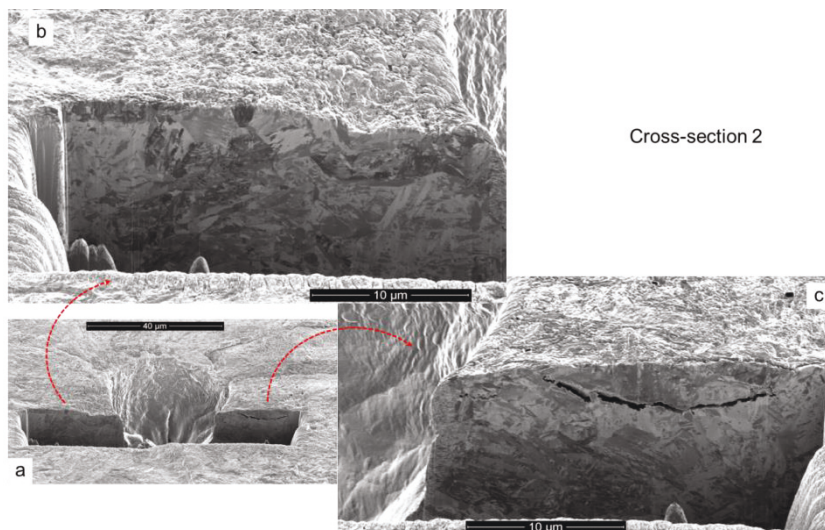
Figure 43. The second milled section, where (a) is the overview, and (b) is the left side and (c) is the right side. All images are taken with ion imaging.

In the right side of the cross-section 2 (

Figure 43(c)) there is a secondary crack which provides an opportunity to investi-
gate both microstructure sides of a very small crack that initiated and grew close
to the subsurface inclusion. The left side of the inclusion hole (
Figure 43(b)), where the milled cross-section shows a step in the fracture surface
where the small crack was growing away from the inclusion.

5. Discussion

5.1 Anisotropy, inclusions and fatigue endurance limit

The fatigue limit of the axial test bars of the forged steel roll was higher when compared to the tangential test bars. The tangential test bars were taken normal to the forging direction which means that they would have elongated grains as well as inclusions; this would explain why the fatigue limit is lower in that direction as well. There is also a significant difference in the scatter of the fatigue test results. A larger amount of scatter in the tangential fatigue test bars is calculated according to two types of analysis. However, the binomial analysis gave an average fatigue limit that is larger, as well as a smaller amount of scatter for the tangential test bars than the MML method. One reason for this is that the tangential test bars have a calculated standard deviation that is more than twice as large as the calculated standard deviation of the axial test bars, and the use of a staircase step size of 5 MPa is not large enough to accurately measure the standard deviation of the fatigue limit. The step size for a staircase test should be close to the true standard deviation of the fatigue limit to properly calculate it according to the MML method. The step size used for the tests was half of the calculated standard deviation for the axial test bars and around 1/7 of the calculated standard deviation for the tangential test bars.

Another reason for the difference in the results between the different methods is that the binomial analysis takes into consideration all of the fatigue tests bars used in testing whereas the MML method uses only the smaller group to calculate the fatigue limit as well as the scatter. This gives an incomplete picture of the true values and can give different results depending on the situation.

The effect of inclusions on the fatigue limit of steels has been shown to be detrimental. The larger amount of scatter in the distribution of the inclusion $\sqrt{area}$ in the axial test bars compared to the tangential test bars is mainly due to the occurrence of a single large inclusion that was the largest of all inclusions that were found in the steel. This inclusion is likely exogenous in nature, meaning that its occurrence is not due to the cleanliness of the steel, but rather was in the steel due to the casting process of the forged steel roll.

Figure 44 illustrates the effect that the inclusions have on the fatigue limit of the steel. The circles illustrate the size of the inclusions located at the site of fatigue crack initiation. The relationship in-between the size of the inclusion and the fatigue life is shown in Figure 44. This figure illustrates a relationship between lower fatigue limit as well as a larger amount of scatter with a population of larger inclusions.
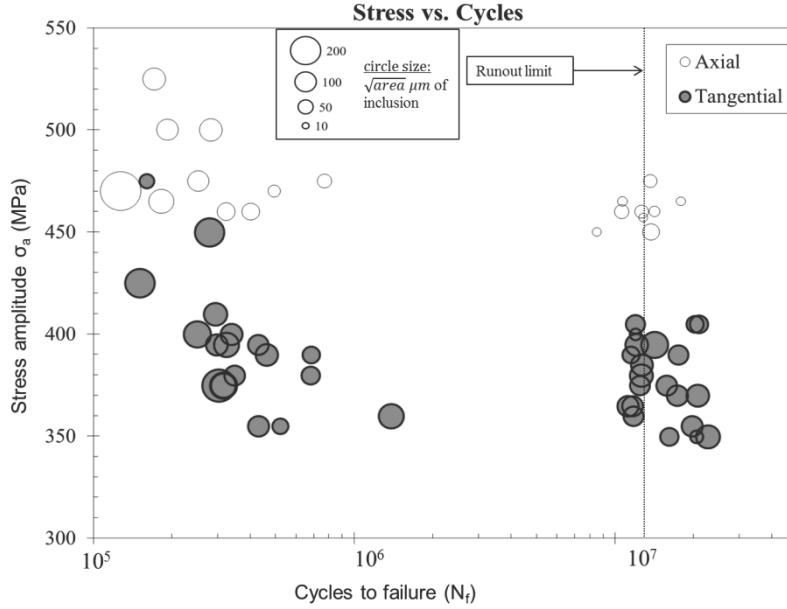
Figure 44. A stress vs. cycle graph where the area of the inclusion found at the site of fracture initiation is shown as the spot size. The results are from the steel studied in publication (I) taken from an industrial forged steel roll.

Using the microhardness of the matrix of the steel along with the maximum inclusion predicted by the extreme value distribution of the inclusions we can use the Mura-kami-Endo model to predict the lower fatigue limit of the steel. The upper limit of fatigue limit can be calculated from the microhardness of the steel. The relationship is given as:

$$\sigma_{wu} = 1.6 \cdot HV \pm 0.1HV \tag{23}$$

Using equation (23) the result of 514.3 ± 32.1 MPa is obtained for an upper limit of fatigue limit for the forged steel roll. The lower fatigue limit was calculated by using equation (17).

Comparing the upper fatigue limit to the actual calculated fatigue limits of both meth-ods shows the amount of the decrease in the fatigue limit. The axial test bars are 51 MPa below the upper limit, and the tangential test bars are 144 – 128 MPa below the upper fatigue limit. The difference in the fatigue limit between the axial and tangential test bars is in agreement with other studies that have tested the aniso-tropic fatigue properties of steel [85,86].

The extreme value analysis of the inclusions from all the polished specimens pro-vided an estimate that is within 4 µm of the average inclusion located on the fracture

surface. This indicates that the extrapolation of the extreme value distribution calculated for the inclusions located on the polished specimen is accurate in predicting the average inclusion size causing fatigue failure. The estimated inclusion for the axial polished surface is accurate as well when the exogenous inclusion is not considered. The tangential polished specimen results are more conservative and estimate larger inclusions than what were actually found on the fracture surface.

In publication (I) The analysis of the average size and average aspect ratio of all of the inclusions that were studied on the polished specimens indicate a clear anisotropic nature of the steel studied. The average size of the inclusions found on the X-plane (corresponding to tangential test bars) is 30.4 μm^2 and average aspect ratio is 1.71 (with a value of one representing a perfect circle). The average size of the inclusions found on the Y-plane (corresponding to axial test bars) is 21.5 μm^2 and the average aspect ratio is 1.63. This difference in the average size and aspect ratio is in agreement with the difference in size of the inclusions found on the fracture surfaces as well as the anisotropic nature of the fatigue limit for the different test bars.

A difference in the PDF of the maximum inclusions on the fracture surfaces is observed when dividing the inclusions into two separate groups. One group comprised of inclusions that caused fatigue crack growth and failure before the runout limit of 10^7 cycles, and the other group being the inclusions that were found on the fracture surface of the runout test bars. The comparison of these two groups can be seen in Figure 45. This figure shows the estimated probability density that was estimated from the histogram plots of the inclusions using the ks-density smoothing kernel in MATLAB.

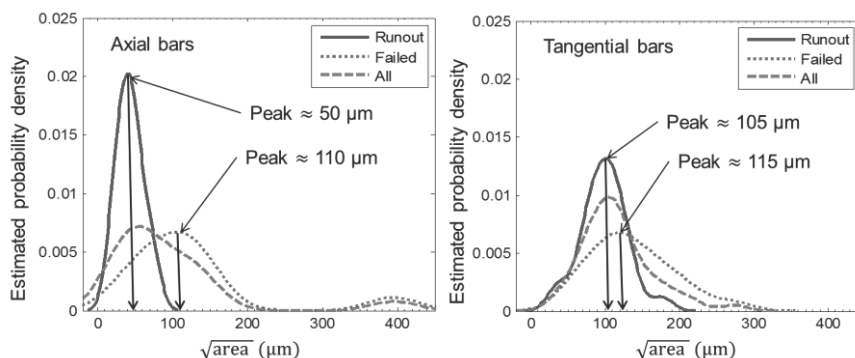Figure 45. The estimated probability density of the inclusion square root area in μm located on the fracture surfaces of the fatigue test bars. The results are from the steel studied in publication (I) taken from an industrial forged steel roll.

Figure 45 shows that the location of the 'All' inclusion peak for tangential test bars is around 110 μm, and for both axial and tangential test bars the Failed peak is

located around 110-115 µm. The fact that the 'All' inclusion distribution peak location in the tangential test bars is almost the same as the failure peak location indicates that the maximum inclusions in the tangential fatigue test bars caused a greater decrease in the fatigue limit and an increase in the amount of scatter.

5.2 Small crack growth

The experimental results of publications (III) and (V) are in agreement with the general results that have been published in earlier studies [80,84,87-89]. The variability along with the faster growth rate of small cracks is evident in Figure 24. This variability is interesting due to the fact that it is the result of reliable measurements obtained with a SEM and that all the data in this figure comes from one fatigue test bar. Therefore the results provide a good picture of the inherent scatter of small crack growth rate that occurs in the microstructure since other variables such as different specimen variability along with possible changes in testing conditions do not contribute to the results.

The organization of the data in Figure 24 according to cycles count shows the variation between slow and fast crack growth rates. The data shows that the cracks grow at faster rates either as they initiate or after they start to grow again after an arrest. It also shows that the growth rate turns into a steady state of growth once the crack grows large enough.

The good correlation between the inclusions and FIB notch thresholds shown in Figure 21 shows that the use of FIB notches as initial defects is a good and relevant way to test the initiation and growth of small cracks in high-strength steels. This is seen as well in Figure 22 where the correlation between defect or crack size versus the stress amplitude shows that there is no decreasing trend for the inclusions or the FIB-milled notches. Rather all these data points are close to the fatigue limit, which means that the studied defect sizes are below the limit for decreasing fatigue limit as function of defect size. The thresholds obtained for the drilled holes indicate that such holes act well as conservative simulations of inclusions. One difference besides the shape in between the FIB-milled notches and the drilled holes is the residual stresses that are introduced by the mechanical removal of material. The ability to quantify or measure this difference is difficult. The other important contributing factor of drilled holes is the difference in shape from the FIB-milled notches. The holes used in this study are equal in depth as in width whereas the FIB notches have a smaller depth when compared to width. The drilled hole will also concentrate the stress into a larger area when compared to the notch due to geometrical factors which means that crack growth will more likely occur when considering a weakest link approach. This means that the size of the volume of material affected by the stress concentration of the hole is larger than that of the notch. Other shape differences include the sharp corners in the drilled hole which may play a crucial role in

early crack initiation and growth. Such mechanically made sharp corners are not present in FIB-milled notches.

5.3   Small cracks, ODA, and microstructure

5.3.1   Fractography

The type of fracture surface referred to as the ODA has been studied in detail. The ODA circled in Figure 36 shows similar fracture surface features as the ones shown in Ref. [20], and when comparing images in Figure 36 and Figure 37 we clearly see similar features that are common among ODA fracture surfaces.

The fracture surface images taken from 100Cr6 bearing steel test bars shown in Figure 40 and Figure 41 do not show as clear an ODA area for which there are several reasons. The 100Cr6 bearing steel is high-strength steel with a much finer grain structure. This can also be seen in the ion images of the milled cross-sections shown in Figure 38 for the 34CrNiMo6 QT(A) steel and in Figure 42 for the 100Cr6 bearing steel. The comparison of these figures shows that the sub-grain structure is noticeably finer in the 100Cr6 bearing steel than in the 34CrNiMo6 QT(A) steel. Since the microstructure is finer, the fracture surface created by a crack following the microstructure will also be finer and will not show as clear lath like structures shown in Figures 37, 38, and 39.

In Figure 40 a weak correlation can be seen between the size of inclusion (also ΔK on y-axis) and endurance. In addition to inclusion size, properties of the metal matrix around the inclusion and configuration of multiple cracks can affect early growth of the crack [84,90]. An influence of adjacent grain orientations has been demonstrated by numerical mesoscale models [91,92]. The correlation between microstructure and crack path are in line with such models. In addition, microstructure may affect through initiation, simultaneous growth and interaction of multiple cracks.

Our fractographic observations reveal the role of multiple crack initiation on slightly different planes. The asymmetrical crack growth that is observed around the inclusion (Figure 41) shows effects of the microstructure and/or multiple crack initiation on the crack path and direction. The fish eye around the inclusion also tells us that the fatigue crack did not propagate directly toward the surface rather obliquely towards it while growing slower on the opposite side of the inclusion, where overlapping of multiple cracks is shown. It is possible that the original initiation of the crack growth into the ODA toward the surface caused a growing stress concentration on the opposite side of the inclusion and initiated cracks on different planes on the other side before the first crack had grown round the circumference.

72

It is worth of noting that the longest life in Figure 40 is associated with a medium size inclusion less than 100 µm below the specimen surface. The fracture of the fatigue test bar shown in Figure 41 shows how three cracks have grown on adjacent planes before coalescence. This has led to a non-symmetrical crack (marked by the fish eye pattern) and retarded growth, in particular on the side where crack "3" has grown on a separate plane still when crack "1" reached the open surface. Similar "butterfly" looking marks around inclusions on UHCF fracture surfaces are commonly seen in literature and also in other inclusions shown in Figure 40.

In summary fatigue cracks do not always initiate exactly at the equator of a spheroid inclusion and several of them initiate to be later coalesced. Depending on the configuration, notable retardation of growth may result and affect the obtained fatigue life. It is possible that in some cases crack arrest occurs at the most critical inclusion and thus fatigue limit will be affected. However, unless such crack arrest can be confirmed, any proof on a correlation with the fatigue limit cannot be presented – just an effect on endurance.

5.3.2   FIB milling

In the quenched and tempered 34CrNiMo6 steel the crack shows a clear preferential growth direction along the martensite laths in the sub-grain microstructure. The pictures in Figure 37 – 40 show that the ODA was formed on the right hand side of the inclusion where horizontal martensite laths can be seen below the ODA region parallel to the direction of crack growth. The lengths of these martensite laths are close to the average prior austenite grain size. They are probably among the first ones to form across the whole prior austenite grain in question. We assume that the crack has first grown and that ODA was formed on this side, where the microstructure provides the most preferential direction for crack growth. Thus, our observations on the preferential crack paths from surface notches (Figure 35) and subsurface inclusions (Figure 38, Figure 42, and 43) are in agreement. Furthermore, an additional explanation to the formation and origin of the ODA is proposed based on the connection to microstructure.

The FIB milling performed on the test bar of 100Cr6 bearing steel showed a finer microstructure than that of the 34CrNiMo6 QT(A) steel. There was evidence of the crack growth direction being influenced by the martensite lath sub-grain microstructure as well as the grain structure. This is shown in Figure 42 where the step in fracture surface is due to either a large martensite lath or a difference in grain structure. In Figure 43(c) secondary crack is observed near the inclusion underneath the actual fracture surface. The crack follows the martensite lath structure until a turning point where the surrounding microstructure changes and the crack changes the direction of growth.

5.3.3   Hydrogen, microstructure and ODA

Earlier work by Murakami et al. has shown that there is a link between the formation of the ODA and hydrogen trapped by the inclusion [22,28,56-62]. A lowering of the threshold stress intensity range by hydrogen for cracks initiating from inclusions has been shown [93]. On the other hand, little hydrogen exists in the steel matrix at milled surface notches. This may explain, why no ODA areas were observed around the FIB notches. However, the hydrogen content of our specimens is not studied. Neither did we search for ODA from the surface notched specimens because we were focusing on the interaction of the small cracks with the microstructure. Nagao et al. and others have studied the interaction of hydrogen and martensite laths [94]. They showed that the presence of hydrogen during monotonic loading caused cracks to preferentially grow along the prior austenite grain or martensite lath boundaries. One other important matter to understand when comparing a non-metallic inclusion with a FIB notch is that the notch is randomly placed into the surface of the test bar, whereas the inclusion is solid in the steel during the steel production process when the steel itself is still molten. This means that there are interactions that take place when the steel solidifies around the inclusion and may be a key reason why there are ODA formations around the inclusion.

Studies such as Ref. [95] show that there may be some kind of grain refinement that takes place around inclusions during the fatigue life. Whereas other studies have concentrated on the fact that the crack growth takes place usually in a vacuum inside the test bar and shown that crack growth in vacuum has a decreased rate when compared to the tests done in air [96]. While the effect of the crack growing in a vacuum certainly does impact the growth of the crack, the effect of the microstructure is critical. The former study used FIB milling to observe the microstructure and it is possible that the fine grains or grain refinement observed was from redeposition of the milled steel by the FIB. Some redeposition in the form of very fine grains is usually observed when milling larger cuts with the FIB.

In our study it was observed that crack growth begins within a region besides the inclusion, later seen as ODA on the fracture surface. It is also observed that the initiation and early growth of the crack are affected by the martensite lath and packet orientation.

The referenced earlier results and our observations are in agreement. Two main factors together affect the early growth of the cracks from the inclusion: the hydrogen trapped and the microstructure around the inclusion. These two factors work together to form the fractographic feature known as ODA on the fracture surface around the inclusions in high-strength steel specimens with ultra-long fatigue lives.

5.4   Small crack growth and compressive loading

The previous studies [53-55] about the effects of compressive loading on fatigue crack growth can be seen to apply also for small cracks in the steel that was studied here. It was measured that increasing the compressive loading for a crack can reinitiate its growth. This is due to the fact that increasing the compressive portion of the loading in constant amplitude testing decreases the ΔK_+ or K_{max} threshold for the crack growth. The experimental work reported here is unique due to the new tools and methods that were employed to monitor and measure small fatigue crack growth under these unique conditions. For this reason there are almost no comparable data that could be used for comparison of the results reported in this study.

The growth rates of small cracks under large compressive cyclic loads are slower when comparing their respective da/dN vs ΔK_+ or K_{max} values. A possible reason for this is that the compressive loading does not affect the crack growth the same way as the tensile portion of the loading does. Rather the compressive loading affects the crack growth through the bulk response of the material along with the full reversal or sharpening of the portion of the crack tip that is held open by the deformations of the plastic zone ahead and around the crack tip. The scale with which the compressive loading affects this could be material dependent. The effectiveness of compressive loading is reducing as the amount of compressive loading is increased.

The saturation of the effect of the compressive loading does not remove the challenges that the increase of the compressive loading has on the initiation and growth of cracks. It has been shown that initiation and crack growth can occur if the compressive portion of the loading is increased. The decrease in the ΔK_+ or K_{max} in the crack arrest is around 12% less for cracks at R = -2 when compared to cracks at R = -1. This is in agreement with the crack growth data at higher growth rates than at crack arrest where the influence of increasing the compressive loading from R = -1 to R = -2 will decrease the ΔK_+ or K_{max} required for crack growth by around 10 to 12%.   If examined from the crack growth rate point of view the growth rate is increased by a factor of around 4 when doubling the compressive loading from R = -1 to R = -2. This indicates that the mechanism through which it affects the crack growth is possibly caused by the removal of crack closure or crack tip sharpening. Once the compression portion of the loading has enhanced the crack growth through these mechanisms, a further increase in compressive loading has less of an effect on the crack growth.

Conclusions

The distribution of non-metallic inclusions in steel is affected by the anisotropy caused by forging. This effect is then mirrored by a lower fatigue limit with a larger amount of scatter in the steel for test specimen taken normal to the forging direction. The estimation of the best distribution for the extreme value theory showed that the Gumbel distribution is best suited to predict the possible largest inclusion in a critical volume for the forged steel studied.

Crack paths around non-metallic inclusions and surface notches were studied in high-strength steels. Fatigue testing was done on specimens with small FIB notches. The cross-sections of the cracks showed that the small cracks tended to follow the martensite laths and packet boundaries.

The fractographic analysis of the non-metallic inclusions indicated that the ODA forms around the inclusion and that there can be several cracks that initiate around the inclusion on different planes. This multiple crack initiation can cause crack arrest due to cracks growing perpendicularly on different planes.

A connection between the microstructure and growth path of small cracks is demonstrated. The general preferential growth direction and formation of "optically dark area" (ODA) can be linked to adjacent grain orientations and sub-grain structures such as martensite lath and packet orientation. Local martensite lath packets in the microstructure surrounding a non-metallic inclusion together with the presence of hydrogen trapped around the inclusion provide an explanation to the formation and origin of the ODA.

The crack path observations show that the behaviour of small cracks is similar near the fatigue endurance limit for FIB notches and non-metallic inclusions. Using this information it is possible to use the measured crack growth data to model cracks growing from inclusions. This provides the ability to model the crack growth rate and fatigue life for a component where the non-metallic inclusion is the critical defect in the steel.

The use of FIB notches as small crack initiators in round test bars provides a reliable method of obtaining small crack growth data that correlates well with the results from test bars that failed from non-metallic inclusions. The microscopic observation of small crack growth from FIB notches during testing is a useful test method for small crack growth observation and can provide results for many loading ratios. The results are in line with previous studies of small crack growth showing a large variability in the crack growth rate as well a decrease in crack size that corresponds with a decrease in ΔK required for crack initiation.

Examining small crack growth using in-situ optical measurement of surface cracks in high-cycle fatigue using multiple test bars with small notches gives unique insights into the initiation and growth of small cracks in HCF. The results show that small crack growth occurs near the fatigue endurance limit of the studied quenched and tempered steel through a process of an accelerated crack growth immediately after initiation. After this brief initiation and accelerated growth of the small crack there follows a period of very slow growth until the large crack growth threshold is reached.

The comparison of small crack behavior at different R-ratios indicates that a good correlation can be obtained by only using the positive portion of the stress amplitude for small cracks. Compressive loading decreases the ΔK_+ or K_{max} threshold for small crack growth and increases the crack growth rate of small cracks. This effect is more pronounced when increasing from R = -1 to R = -2, than when increasing from R = -2 to R = -3.73.

The main conclusions are as follows:

- Anisotropy affects inclusion size and distribution and therefore the fatigue endurance limit and scatter.
- Small cracks initiating from FIB notches and non-metallic inclusions follow the local microstructure.
- Small cracks, at first, initiate quickly and then grow very slowly below and close to the threshold of large crack growth.
- The parameter ΔK_+ works well to compare the crack growth rate of small cracks in the studied quenched and tempered steel.
- Crack arrest ΔK_+ or K_{max} thresholds are lower for cracks with higher compressive loading.
- Increasing only the compressive portion of loading can reinitiate arrested small cracks.
- The ΔK_+ or K_{max} values for small cracks are lower for similar crack growth rates under larger compressive loads.

Acknowledgements

References

[1] H. Kitagawa and S. Takahashi, "Applicability of fracture mechanics to very small cracks or crack in the early stage," in *Proceedings of the Second International Conference on Mechanical Behaviour of Material*, 1976.

[2] R. Smith, "On the short crack limitations of fracture mechanics," *International Journal of Fracture,* vol. 13, pp. 717-720, 1977.

[3] D. Taylor, "Fatigue of short cracks: the limitations of fracture mechancis," in *The Behaviour of Short Fatigue Cracks, EGF Pub. 1*, K. J. Miller and E. R. de los Rios, Eds., London, Mechancial Engineering Publications, pp. 479-490, 1986.

[4] K. Tanaka, Y. Nakai and M. Yamashita, "Fatigue growth threshold of small cracks," *International Journal of Fracture,* vol. 17, pp. 519-533, 1981.

[5] Y. Murakami and M. Endo, "Effect of hardness and crack geometry on delta K threshold of small cracks," *Journal of the Society of Materials Science, Japan,* vol. 35, pp. 911-917, 1985.

[6] S. Suresh and R. Ritchie, "Propagation of short fatigue cracks," *International Metal Reviews,* pp. 445-476, 1984.

[7] A. McEvily, D. Eifler and E. Macherauch, "An analysis of the growth of short fatigue cracks," *Engineering Fracture Mechanics,* vol. 40, pp. 571-584, 1991.

[8] A. J. McEvily, M. Endo and Y. Murakami, "On the square root area relationship and the short fatigue crack threshold," *Fatigue and Fracture of Engineering Materials and Structures,* no. 26, pp. 269-278, 2003.

[9] P. Lukas and L. Kunz, "Small cracks—nucleation, growth and implication to fatigue life," *International Journal of Fatigue,* vol. 25, pp. 855-862, 2003.

[10] W. Duckworth and E. Ineson, "The effects of externally introduced alumina particles on the fatigue life of En24 steel," *Clean Steel 77 (Iron Steel Inst.),* pp. 87-103, 1963.

[11] R. Kiessling, "Non-metallic inclusions in steel, Parts I-IV," *The Metals Society,* 450 p., 1978.

[12] R. Kiessling, "Clean steel: a debatable concept," *Metal Science,* vol. 14, pp. 161-172, 1980.

[13] R. Kiessling, "Non-metallic inclusions in steel, Part V," *The Institute of Metals,* 194 p., 1989.

[14] Y. Murakami and M. Endo, "Quantitative evaluation of fatigue strength of metals containing various small defects or cracks," *Engineering Fracture Mechanics,* vol. 17, pp. 1-15, 1983.

[15] J. Cogne, B. Heritier and J. Monnot, "Cleanness and fatigue life of bearing steels In: Clean Steel 3," Balatonfured, Hungary, The Institute of Metals, pp. 26-31, 1987.

[16] Y. Murakami, S. Kodama and S. Konuma, "Quantitative evaluation of effects of non-metallic inclusions on fatigue strength of high strength steels. I: Basic fatigue mechanism and evaluation of correlation between the fatigue fracture stress and the size and location of non-metallic inclusions," *International Journal of Fatigue,* vol. 11, pp. 291-298, 1989.

[17] Y. Murakami and H. Usuki, "Quantitative evaluation of effects of non-metallic inclusions on fatigue strength of high strength steels. II: Fatigue limit evaluation based on statistics for extreme values of inclusion size," *International Journal of Fatigue,* vol. 11, pp. 299-307, 1989.

[18] Y. Murakami, K. Kawakami and W. Duckworth, Quantitative evaluation of effects of shape and size of artificially introduced alumina particles on the fatigue strength of 1.5Ni-Cr-Mo (En24) steel, *International Journal of Fatigue*, pp. 489-499, 1991.

[19] Y. Murakami and M. Endo, "Effects of defects, inclusions and inhomogeneities on fatigue strength," *International Journal of Fatigue,* vol. 16, no. 3, pp. 163-182, 1994.

[20] S. Beretta, A. Blarasin, M. Endo, T. Giunti and Y. Murakami, "Defect tolerant design of automotive components.," *International Journal of Fatigue,* vol. 19, pp. 319-333, 1997.

[21] S. Beretta and Y. Murakami, "Statistical analysis of defects for fatigue strength prediction and quality control of materials," *Fatigue & Fracture of Engineering Materials & Structures,* vol. 21, pp. 1049-1065, 1998.

[22] Y. Murakami, T. Nomoto and T. Ueda, "Factors influencing the mechanism of superlong fatigue failure in steels," *Fatigue & Fracture of Engineering Materials & Structures ,* vol. 22, pp. 581-590, 1999.

[23] Y. Murakami and S. Beretta, "Small defects and inhomogeneities in fatigue strength: experiments, models and statistical implications," *Extremes,* pp. 123-147, 1999.

[24] S. Beretta and Y. Murakami, "Largest-extreme-value distribution analysis of multiple inclusion types in determining steel cleanliness," *Metallurgical and Materials Transactions B,* vol. 32B, pp. 517-523, 2001.

[25] M. Todinov, "Probability distribution of fatigue life controlled by defects," *Computers and Structures,* vol. 79, pp. 313-318, 2001.

[26] F. Meurling, A. Melander, M. Tidesten and L. Westin, "Influence of carbide and inclusion contents on the fatigue properties of high speed steels and tool steels," *International Journal of Fatigue,* vol. 23, pp. 215-224, 2001.

[27] S. Beretta, G. Chai and E. Soffiati, "A weakest–link analysis for fatigue strength of components containing defects," in *Proceedings of the 11th Int Conf Fract*, Turin, 2005.

[28] Y. Murakami, Metal Fatigue: Effects of Small Defects and Nonmetallic Inclusion, Kyushu University: Elsevier, 2002.

[29] M. Tiryakioglu, "On the size distribution of fracture-initiating defects in Al- and Mg-alloy castings," vol. 476, pp. 174-177, 2008.

[30] N. Cyril and A. Fatemi, "Experimental evaluation and modeling of sulfur content and anisotropy of sulfide inclusions on fatigue behavior of steels," *International Journal of Fatigue,* vol. 31, pp. 526-537, 2009.

[31] K. Wallin, "Statistical aspects of fatigue life and endurance limit," *Fatigue and Fracture of Engineering Materials and Structures,* vol. 33, pp. 333-344, 2010.

[32] M. Tiryakioglu, "Statistical distributions for the size of fatigue-initiating defects in Al–7%Si–0.3%Mg alloy castings: A comparative study," *Materials Science and Engineering A,* pp. 119-125, 2008.

[33] M. Tiryakioglu, "On the size distribution of fracture-initiating defects in Al- and Mg-alloy castings," *Materials Science and Engineering A,* vol. 476, pp. 174-177, 2008.

[34] R. Kiessling and N. Lange, Non-metalic Inclusions in Steel, London: The Institute of Materials, 1978.

[35] A. M. Freudenthal and E. J. Gumbel, "Minimum life in fatigue," *Journal of the American Statistical Association,* vol. 49, no. 267, pp. 575-597, 1954.

[36] S. Beretta and Y. Murakami, "Statistical analysis of defects for fatigue strength prediction and quality control of materials," *Fatigue & Fracture of Engineering Materials & Structures,* vol. 21, pp. 1049-1065, 1998.

[37] S. Beretta and Y. Murakami, "Largest-extreme-value distribution analysis of multiple inclusion types in determining steel cleanliness," *Metallurgical and Materials Transactions B,* vol. 32, pp. 517-523, 2001.

[38] J. W. Dixon and A. M. Mood, "A method for obtaining and analyzing sensitivity data," *Journal of the American Statistical Association,* vol. 43, pp. 109-126, 1948.

[39] K. R. Wallin, "Statistical uncertainty in the fatigue threshold staircase method," *International Journal of Fatigue,* vol. 33, pp. 354-362, 2011.

[40] K. Wallin, R. Voskamp, J. Schmidbauer, H. Ostermeyer and G. Nagel, "Statistical assessment method for the optimization of the inspection need for nuclear steam generators based on existing inspection data," in *20th International Conference on Structural Mechanics in Reactor Technology (SMiRT 20)*, 2009.

[41] M. El Haddad, T. Topper and K. Smith, "Prediction of non propagating cracks," *Engineering Fracture Mechanics,* vol. 11, pp. 573-584, 1979.

[42] M. James and G. Smith, "Crack closure and surface microcrack thresholds some experimental observations," *International Journal of Fatigue,* vol. 5, pp. 75-78, 1983.

[43] M. Chapetti, "Fatigue propagation threshold of short cracks under constant amplitude loading," *International Journal of Fatigue,* vol. 25, pp. 1319-1326, 2003 .

[44] N. Fleck, C. Shin and R. Smith, "Fatigue crack growth under compressive loading," *Engineering Fracture Mechanics,* vol. 21, pp. 173-185, 1985.

[45] S. Suresh, "Crack initiation in cyclic compression and its applications," *Engineering Fracture Mechanics,* vol. 21, pp. 453-463, 1985.

[46] R. Pippan, "The growth of short cracks under cyclic compression," *Fatigue & Fracture of Engineering Materials & Structures,* vol. 9, pp. 319–328, 1987.

[47] R. Hermann, "Fatigue crack growth in ductile materials under cyclic compressive loading," *Fatigue & Fracture of Engineering Materials & Structures,* vol. 17, pp. 93-103, 1994.

[48] K. Kasaba, T. Sano, S. Kudo, T. Shoji, K. Katagiri and T. Sato, "Fatigue crack growth under compressive loading," *Journal of Nuclear Materials,* vols. 258-263, pp. 2059-2063, 1998.

[49] M. Aratani and J. Knott, "The growth of short fatigue cracks ahead of a notch in high strength steel," *Engineering Failure Analysis,* vol. 17, pp. 200-207, 2010.

[50] T. Hsua and Z. Wanga, "Fatigue crack initiation at notch root under compressive cyclic loading," *Procedia Engineering,* vol. 2, pp. 91-100, 2010.

[51] W. Elber, "Fatigue crack closure under cyclic tension," *Engineering Fracture Mechanics,* vol. 2, pp. 37-45, 1970.

[52] W. Elber, "The significance of fatigue crack closure," *Damage Tolerance in Aircraft Strucures,* vol. ASTM STP 486, pp. 230-242, 1971.

[53] F. Silva, "Crack closure inadequacy at negative stress ratios," *International Journal of Fatigue,* vol. 26, pp. 241-252, 2004.

[54] F. Silva, "The importance of compressive stresses on fatigue crack propagation rate," *International Journal of Fatigue,* vol. 27, pp. 1441–1452, 2005.

[55] C. Benz and M. Sander, "Reconsiderations of fatigue crack growth at negative stress ratios: Finite element analyses," *Engineering Fracture Mechanics,* vol. 145, pp. 98-114, 2015.

[56] Y. Murakami, T. Nomoto, T. Ueda and Y. Murakami, "On the mechanism of fatigue failure in the superlong life regime (N>10^7 cycles). Part 1: influence of hydrogen trapped by inclusions," *Fatigue & Fracture of Engineering Materials & Structures,* vol. 23, pp. 893-902, 2000.

[57] Y. Murakami, T. Nomoto, T. Ueda and Y. Murakami, "On the mechanism of fatigue failure in the superlong life regime (N>10^7 cycles). Part II: influence of

hydrogen trapped by inclusions," *Fatigue & Fracture of Engineering Materials & Structures,* vol. 23, pp. 903-910, 2000.

[58] Y. Murakami, H. Konishi, K. Takai and Y. Murakami, "Acceleration of superlong fatigue failure by hydrogen trapped by inclusions and elimination of conventional fatigue limit," *Tetsu-to-Hagane,* vol. 86, pp. 777-783, 2000.

[59] Y. Murakami, N. Yokoyama and J. Nagata, "Mechanism of fatigue failure in ultralong life regime," *Fatigue & Fracture of Engineering Materials & Structures,* vol. 25, pp. 735-746, 2002.

[60] T. Ueda and Y. Murakami, "Effect of hydrogen on ultralong life fatigue failure of a high strength steel and fracture morphology of ODA," *Transactions of the Japan Society of Mechanical Engineers, Series A,* vol. 69, pp. 908-915, 2003.

[61] Y. Murakami and J. Nagata, "Effect of hydrogen on high cycle fatigue failure of high strength steel, SCM435," *Journal of the Society of Materials Science Japan,* vol. 54, pp. 420-427, 2005.

[62] Y. Murakami and J. Nagata, "Influence factors of fatigue design in ultralong life regime and effect of hydrogen on fatigue strength of high strength steel," *Transactions of the Japan Society of Mechanical Engineers, Series A,* vol. 70, pp. 1093-1101, 2005.

[63] H. Uyama, M. Nakashima, K. Morishige, Y. Mine and Y. Murakami, "Effects of hydrogen charge on microscopic fatigue behaviour of annealed carbon steels," *Fatigue & Fracture of Engineering Materials & Structures,* vol. 29, pp. 1066-1074, 2006.

[64] Y. Hong, Z. Lei, C. Sun and A. Zhao, "Propensities of crack interior initiation and early growth for very-high-cycle fatigue of high strength steels," *International Journal of Fatigue,* vol. 58, pp. 144-151, 2014.

[65] T. Sakai, N. Oguma and A. Morikawa, "Microscopic and nanoscopic observations of metallurgical structures around inclusions at interior crack initiation site for a bearing steel in very high-cycle fatigue," *Fatigue & Fracture of Engineering Materials & Structures,* vol. 38, pp. 1305-1314, 2015.

[66] A. Grabulov, R. Petrov and H. Zandbergen, "EBSD investigation of the crack initiation and TEM/FIB analyses of the microstructural changes around the cracks formed under Rolling Contact Fatigue (RCF)," *International Journal of Fatigue,* vol. 32, pp. 576-583, 2010.

[67] T. Olson, R. Lee and J. Morgan, "Contrast mechanisms in focused ion beam imaging.," in *Proceedings of ISTFA '92, 18th International Symposium for Testing and Failure Analysis*, Los Angeles, 1992.

[68] Y.-Z. Wang, R. Revie, M. W. Phaneuf and J. Li, "Application of focused ion beam (FIB) microscopy to the study of crack profiles," *Fatigue and Fracture of Engineering Materials and Strucures,* vol. 22, pp. 251-256, 1999.

[69] Y. Motoyashiki, A. Brückner-Foit and A. Sugeta, "Investigation of small crack behaviour under cyclic loading in a dual phase steel with an FIB tomography

technique," *Fatigue & Fracture of Engineering Materials & Structures,* vol. 30, pp. 556-564, 2007.

[70] Y. Motoyashiki, A. Brückner-Foit and A. Sugeta, "Microstructural influence on small fatigue cracks in a ferritic–martensitic steel," *Engineering Fracture Mechanics,* vol. 75, pp. 768-778, 2008.

[71] E. Keehan, L. Karlsson, H. Bhadeshia and M. Thuvander, "Three-dimensional analysis of coalesced bainite using focused ion beam tomography," *Materials Characterization,* vol. 59, pp. 877-882, 2008.

[72] C. Volkert and A. Minor, "Focused ion beam microscopy and micromachining," *MRS Bulletin,* vol. 32, pp. 389-395, 2007.

[73] Y. Sakai, T. Yamada, T. Suzuki, T. Sato, H. Itoh and T. Ichinokawa, "Contrast mechanisms in scanning ion microscope imaging for metals," *Applied Physics Letters,* vol. 73, pp. 611-613, 1998.

[74] M. Marx, W. Schäf, H. Vehoff and C. Holzapfel, "Interaction of microcracks with selected interfaces: Focused ion beam for a systematic crack initiation," *Materials Science and Engineering A,* pp. 595-601, 2006.

[75] C. Holzapfel, W. Schäf, M. Marx, V. H. and F. Mucklicha, "Interaction of cracks with precipitates and grain boundaries: Understanding crack growth mechanisms through focused ion beam tomography," *Scripta Materialia,* vol. 56, pp. 697-700, 2007.

[76] W. Schaef, M. Marx, H. Vehoff, A. Heckl and P. A. Randelzhofer, "3-D view on the mechanisms of short fatigue cracks interacting with grain boundaries.," *Acta Materialia,* vol. 59, pp. 1849-61, 2011.

[77] J. Nagata and Y. Murakami, "Factors influencing the formation of ODA in ultralong fatigue regime," *Journal of the Society of Materials Science Japan,* vol. 52, pp. 966-973, 2003.

[78] Y. Murakami, T. Nomoto and T. Ueda, "Factors influencing the mechanism of superlong fatigue failure in steels," *Fatigue & Fracture of Engineering Materials & Structures,* vol. 22, pp. 581-590, 1999.

[79] Y. Murakami, T. Nomoto, T. Ueda, Y. Murakami and M. Ohori, "Analysis of the mechanism of superlong fatigue failure by optical microscope and SEM/AFM observations," *Journal of the Society of Materials Science Japan,* vol. 48, pp. 1112-1117, 1999.

[80] N. Couroneau and J. Royer, "Simplified model for the fatigue growth analysis of surface cracks in round bars under mode I," *International Journal of Fatigue,* vol. 20, pp. 711-718, 1998.

[81] Y. Murakami, Ed., Stress Intensity Factors Handbook, Pergamon, 1987.

[82] M. Marx, W. Schäf, H. Vehoff and C. Holzapfel, "Interaction of microcracks with selected interfaces: Focused ion beam for a systematic crack initiation," *Materials Science and Engineering A,* Vols. 435-436, pp. 595-601, 2006.

[83] A. Tesch, R. Pippan, K.-H. Trautmann and H. Döker, "Short cracks initiated in Al 6013-T6 with the focused ion beam (FIB)-technology," *International Journal of Fatigue,* vol. 29, pp. 1803-1811, 2007.

[84] J. Solin, J. Alhainen and P. Varis, "Ultra high cycle fatigue and inclusions in wrought steels," in *Int Symposium on Fatigue Design and Material Defects*, Trondheim, 2011.

[85] E. Pessard, F. Morel, A. Morel and D. Bellett, "Modelling the role of non-metallic inclusions on the anisotropic fatigue behaviour of forged steel," *International Journal of Fatigue,* vol. 33, pp. 568-577, 2011.

[86] J. Ma, B. Zhang, D. Xu, E. Han and W. Ke, "Effects of inclusion and loading direction on the fatigue behavior of hot rolled low carbon steel," *International Journal of Fatigue,* vol. 32, pp. 1116-1125, 2010.

[87] B. Menzel and R. Dauskardt, "Fatigue damage initiation and growth from artificial defects in Zr-based metallic glass.," *Acta Materialia,* vol. 56, pp. 2955-2965, 2008.

[88] M. Roy, Y. Nadot, C. Nadot-Martin, P.-G. Bardin and D. Maijer, "Multiaxial Kitagawa analysis of A356-T6.," *International Journal of Fatigue,* vol. 33, pp. 823-832, 2011.

[89] Y. Yang, H. Ruan, J. Lu, N. Yao, W. Shan and W. Soboyejo, "Development of a microbeam method to investigate the fatigue crack growth mechanisms of submicron-scale cracks," *Experimental Mechanics,* vol. 49, pp. 731-742, 2009.

[90] U. Krupp, H. Knobbe, H.-J. Christ, P. Köster and C.-P. Fritzen, "The significance of microstructural barriers during fatigue of a duplex steel in the high- and very-high-cycle-fatigue (HCF/VHCF) regime," *International Journal of Fatigue,* vol. 32, pp. 914-920, 2010.

[91] E. Mikkola, G. Marquis and J. Solin, "Mesoscale modelling of crack nucleation from defects in steel," *International Journal of Fatigue,* vol. 41, pp. 64-71, 2012.

[92] D. McDowell and F. Dunne, "Microstructure-sensitive computational modeling of fatigue crack formation," *International Journal of Fatigue,* vol. 32, pp. 1521-1542, 2010.

[93] Y. Murakami, T. Kanezaki and P. Sofronis, "Hydrogen embrittlement of high strength steels: Determination of the threshold stress intensity for small cracks nucleating at nonmetallic inclusions," *Engineering Fracture Mechanics,* vol. 97, pp. 227-243, 2013.

[94] K. Nagao, C. D. Smith, M. Dadfarnia, P. Sofronis and I. M. Robertson, "The role of hydrogen in hydrogen embrittlement fracture of lath martensitic steel," *Acta Materialia,* vol. 60, pp. 5182-5189, 2012.

[95] P. Grad, B. Reuscher, A. Brodyanski, M. Kopnarski and E. Kerscher, "Mechanism of fatigue crack initiation and propagation in the very high cycle

fatigue regime of high-strength steels," *Scripta Materialia,* vol. 67, pp. 838-841, 2012.

[96] S. Stanzl-Tschegg and B. Schonbauer, "Near-threshold fatigue crack propagation and internal cracks in steel," *Procedia Engineering,* vol. 2, pp. 1547-1555, 2010.

Small defects are often the cause of fatigue crack initiation and failure. Since the initiation and growth of small cracks is the longest portion of the fatigue life of a machine component it is also the area where the largest increase in performance and quality can be achieved through better understanding and modeling of the material. The prediction of the defect size along with the measurement and analysis of the small crack growth due to fatigue loading is examined in this thesis. The results provide knowledge and guidance to improve the quality and efficiency of engineering structures. The new methods and test results support and improve the modeling and prediction of machine components used in more demanding applications and loading situations.

BUSINESS +
ECONOMY

ART +
DESIGN +
ARCHITECTURE

SCIENCE +
TECHNOLOGY

CROSSOVER

DOCTORAL
DISSERTATIONS